Assembly of Macromolecular Complexes in the Whole-Cell Model of a Minimal Cell

Enguang Fu,[†,‡] Zane R. Thornburg,[¶,§,⊥] Troy A. Brier,[†,⊥] Rong Wei,[‖,‡] Bo Yuan,[‖,‡] Benjamin R. Gilbert,[†] Shulei Wang,[‖,‡] and Zaida Luthey-Schulten[*,†,‡,¶,§]

†*Department of Chemistry, University of Illinois at Urbana-Champaign, IL, USA*

‡*National Science Foundation Science and Technology Center for Quantitative Cell Biology, Beckman Institute for Advanced Science and Technology, University of Illinois at Urbana–Champaign, Urbana, IL, USA*

¶*Beckman Institute for Advanced Science and Technology, University of Illinois at Urbana–Champaign, Urbana, IL, USA*

§*Cancer Center at Illinois, University of Illinois at Urbana–Champaign, Urbana, IL, USA*

‖*Department of Statistics, University of Illinois at Urbana-Champaign, IL, USA*

⊥*These authors contributed equally*

E-mail: zan@illinois.edu

Abstract

Macromolecular complexes in the genetically minimized bacterium, JCVI-syn3A, support gene expression (RNA polymerase, ribosome, degradosome), metabolism (ABC transporters, ATP synthase) and chromosome dynamics. In this work, we further incorporate the assembly of 21 unique macromolecular complexes into the existing whole-cell kinetic model of Syn3A. The synthesis and translocation of protein subunits in membrane complexes occur through distinct pathways. A range of assembly rates were considered to guarantee a high yield of assembly given the existing time scales

of the gene expression with derived formula to rationalize the choice. By alleviating the undesired dead-end intermediates in ATP synthase assembly, the efficiency was improved, while the heterogeneity of subunit synthesis at the single-cell level greatly undermine it. The assembly of RNA polymerase, ribosome, and degradosome influence the speed and efficiency of protein synthesis. Collectively, this model predicted time-dependent cellular behaviors consistent with experiments. A deep learning analysis of the simulated time-dependent concentrations of 148 intracellular metabolites allowed the construction of a trajectory tree from which three distinct metabolic phenotypes were identified in the population of ~ 100 cells considered.

Introduction

The minimal cell, JCVI-syn3A, is a bacterium with a chemically synthesized genome derived from the parental organism *Mycoplasma mycoides subsp. capri* strain GM12.[1,2] Syn3A exhibits a doubling time of less than two hours[2–4] and possesses the smallest genome known among autonomously replicating organisms. This minimal genome comprises 543 kbp, encoding 455 protein-coding genes, 6 rRNA-coding genes, and 29 tRNA-coding genes. Of the protein-coding genes, roughly 90 genes have unknown functions, the lowest proportion among model organisms such as *Mycoplasma pneumoniae* and *Escherichia coli*. During the reduction over half of the M. mycoides genome was removed including the majority of regulation and transcription factors.[2,5]

In 2022,[6] we integrated kinetic parameters, omics data,[2] and spatial data (cell size and ribosome distribution) from cryo-electron tomography (cryo-ET)[7] to construct a comprehensive whole-cell model (WCM) of Syn3A. The genetic information processes of DNA replication, transcription, translation, and mRNA degradation[8] were treated stochastically using chemical master equations (CMEs), while the essential metabolism[2] with thermodynamically consistent kinetic parameters[6] was deterministically simulated using ordinary differential equations (ODEs). To simulate cooperative dynamics between two networks, a hybrid

CME-ODE algorithm was used in which the simulations were discretized in time, and information between them occurred at a prescribed communication time.[6,9] This approach enabled the calculation of time-dependent abundances of all genes, RNAs, and proteins, and metabolites. We simulated trajectories throughout the cell cycle and investigated the balance of energy cost and metabolic resources.[6] This early model used probabilistic factors obtained from short 3D simulations using the static morphology and ribosome distributions obtained from the cyro-electron tomograms. It also used abundances of specified subunits from the proteomics data to represent the complexes and did not consider formation of intermediates which we now consider.

In all organisms including Syn3A, key macromolecular complexes mediate essential cellular processes. In genetic information processing, RNA polymerase (RNAP) and ribosomes decode genetic information into mRNAs and functional proteins via transcription and translation, respectively. Degradosomes, a loose complex of endoribonuclease, exoribonuclease, and a few glycolytic enzymes compete with ribosomes for the binding and processing of mRNA, and without regulation factors control protein generation. Several essential complexes interact with chromosomes and facilitate chromosome partitioning during cell division.[10] The essential metabolism of Syn3A depends on the activated transport of (deoxy)nucleosides, amino acids, vitamins and fatty acids into the cell by membrane complexes with multiple subunits. The Sec translocon is a vital membrane-embedded machinery for translocation of transmembrane proteins and secretory proteins.[11] ATP synthase has to assemble eight kinds of subunits in varying stoichiometry in order to function properly. In nucleotide metabolism, ribonucleoside-diphosphate reducatese (RNDR) converts ribonucleoside diphosphates to deoxyribonucleoside diphosphates to help balance the conversion NTP to dNTP when uptake of (deoxy)nucleosides is insufficient.

Investigation of assembly pathways typically begins with the identification of assembly intermediates using imaging,[12,13] chromatography,[14] and mass spectrometry,[15] followed by the elucidation of the preferred pathways through *in vitro* reconstruction[16,17] and time-delayed

assembly experiments.[18] Quantification of the bimolecular binding rates along the assembly pathways is difficult because of the diverse protein-protein interactions and numerous assembly intermediates. Taking into account the different dimensions, the 3D cytoplasm, the 2D membrane, and the 1D DNA, and their coupling within a single cell,[19,20] the assembly landscape is "complex". One example is the classic investigation on ribosome biogenesis. The assembly of bacterial ribosomes (ribosome biogenesis) is crucial for protein synthesis and is highly relevant to cell growth. The bacterial ribosome comprises a small subunit (30S SSU) and a large subunit (50S LSU), each of which is a ribonucleoprotein complex that assembles independently.[13,15,17,21–23] The assembly pathways of both subunits are hierarchical as indicated by the pioneering exploration of the SSU by Nomura *et al.*[21] and in the LSU by Nierhaus *et al.*[22] and Williamson *et al.*[13] For SSU, 16S rRNA is first bound by primary binding proteins, and then secondary and tertiary ribosomal proteins bind by interacting with rRNA and bound proteins, called thermodynamic dependencies. Similar hierarchy was also found for LSU but with less clear separation in the order. In addition to the order restricted by thermodynamic dependencies, parallel pathways exist to offer redundancy in the event of misfolding of rRNA under various physiological conditions.[13,23] In 2015, we simulated the *in vivo* SSU assembly in *E. coli* with coupled transcription, translation, and mRNA degradation using stochastic reaction-diffusion master equations with rigorous parameterization of ribosome subunits binding rates by fit to the pulse chase data from the Williamson laboratory.[24] The SSU assembly pathways comprising 145 intermediates and multiple parallel pathways are shown in Figure 1(a). Later, the model was extended to include a simplified treatment of cell growth, DNA replication, and cell division.[25] Here we test if the assembly pathway can be further reduced to a hierarchical one with only 19 intermediates.

In the previous Syn3A WCMs, we used representative subunits to specify the abundance of complete macromolecular complexes. For example, RNAP subunit α encoded by gene *rpoA*/0645 was picked for RNAP, and degradosome subunit RNase Y encoded by *rny*/0359 degradosome. For enzymatic protein complexes in metabolism, the Gene-Protein-Reaction

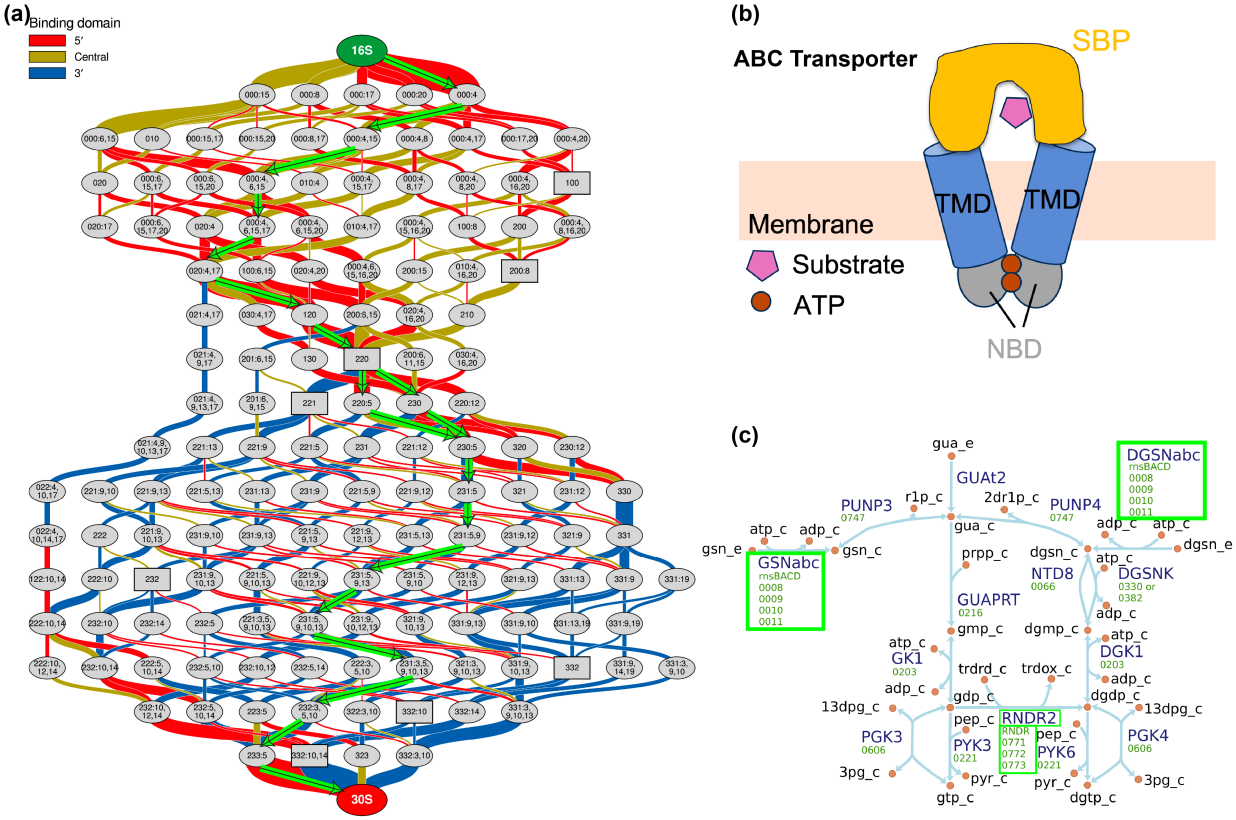

Figure 1: Ribosome 30S small subunit (SSU) assembly pathway, domain composition of ABC transporters, and nucleotide metabolism in Syn3A. (a) Hierarchical and parallel assembly pathway of SSU with 145 assembly intermediates,[26] where the thickness of edges represents the fluxes. The marked green pathway was the reduced assembly pathway with the largest flux and 19 intermediates. Adapted with permission from Earnest, T. M.; Lai, J.; Chen, K.; Hallock, M. J.; Williamson, J. R.; Luthey-Schulten, Z. Toward a Whole-Cell Model of Ribosome Biogenesis: Kinetic Modeling of SSU Assembly. *Biophysical Journal* **2015**, *109*, 1117–1135. Copyright 2015/ELSEVIER. (b) Typical domain composition of ABC transporter in Gram-positive organisms. SBP: Substrate Binding Protein, TMD: Transmembrane Domain, NBD: Nucleotide Binding Domain. (c) Nucleotide metabolism of GTP and dGTP with reactions catalyzed by protein complexes circled. ABC transporter rnsBACD import guanosine and deoxyguanosine in GSNabc and DGSNabc reactions.

(GPR) rules[2] were applied to catalyzed reactions. For example, ABC transporters in Gram-positive organisms have a domain composition of two peripheral nucleotide binding domains (NBD) that provide ATP hydrolysis, two transmembrane domains (TMD) that form the permease channel, and one substrate binding protein (SBP) that delivers substrates to TMDs[27] as shown in Figure 1(b). The nucleoside ABC transporter rnsBACD comprises 4 distinct subunits of proteins RnsD/0008 (TMD), RnsC/0009 (TMD), RnsA/0010 (2NBDs), and RnsB/0011 (SBP) with 1:1:1:1 stoichiometries, where protein subunit RnsA/0010 correpsonds to two NBDs.[28] Previously, we used the AND GPR rule on two subunits RnsC/0009 and RnsA/0010 to take their minimum to represent the abundance of the ABC transporter rnsBACD in the membrane when simulating the import of nucleosides in the nucleotide metabolism marked in Figure 1(c). For completeness, the functional roles of the complexes in this study are listed in Table 1, and visualized in metabolic maps as Figure S1.

The complexity of *in vivo* macromolecular complex assembly arises from the following aspects. First, the complicated assembly landscape consists of the composition of the macromolecular complex, the pathways that depend on the variation in affinity between the protein subunits, and rates for each bimolecular binding step. Second, the translocation of membrane-related proteins, that is, the placement of proteins in the membrane, occurs through an orchestrated network that includes actively translating ribosomes (ribosome-nascent chain complexes, i.e. RNC), targeting factors, and membrane-embedded insertases and translocons.[29,30] Lastly, protein assembly must be dynamically consistent with protein synthesis from gene expression along the cell cycle. Slow assembly leads to the accumulation of unassembled subunit precursors that will form protein aggregates and hinder other cellular activities.[31]

The association kinetics of 3D diffusive proteins have been extensively studied through a series of theoretical works,[32,33] whereas much less is known about the kinetics of membrane protein interactions. In the pioneering WCMs of *Mycoplasma genitalium*[34] and *E. coli*,[35] the formation of protein complexes was simplified as an one-step reaction from multiple

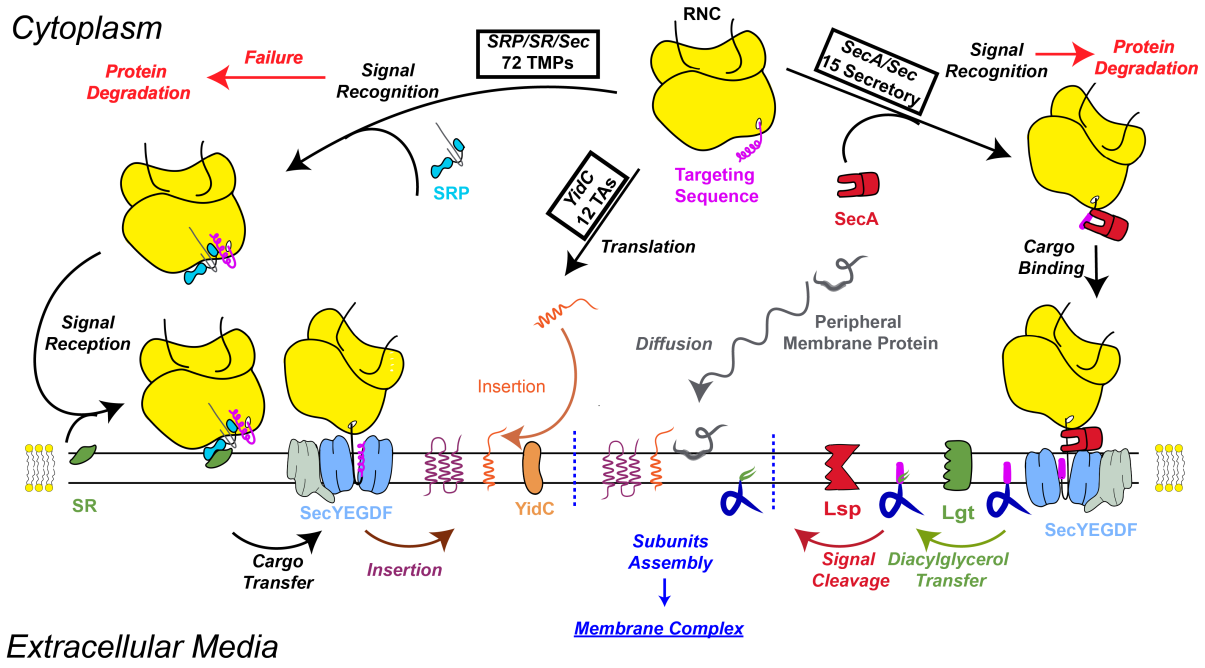

Figure 2: Translocation pathways for transmembrane proteins, and lipoproteins, and peripheral membrane proteins in Syn3A. Protein subunits' localizations are classified as the cytoplasm, peripheral membrane, transmembrane, and secretory in Syn3A. Most transmembrane proteins (72/84) are co-translationally inserted via the SRP/SR/Sec pathway. 12 tail-anchored (TA) membrane proteins can be post-translationally inserted via YidC.[30] Secretory proteins are translocated via the SecA/Sec translocon; 13 lipoproteins, after modification anchor to and diffuse within the outer membrane leaflet, while 2 others are secreted to extracellular space. The failure of targeting in cotranslational translocation is considered and will lead to protein degradation by transmembrane protease, FtsH. Peripheral membrane proteins reversibly associate with the membrane by binding to transmembrane proteins and/or membrane lipids, thereby carrying out their functions at the membrane interface. Proteins in cytoplasm (omitted) are translated and then function in the cytoplasm. Adapted with permission from Du Plessis, D. J.; Nouwen, N.; Driessen, A. J. The Sec translocase. *Biochimica et Biophysica Acta (BBA) - Biomembranes* **2011**, *1808*, 851-865. Copyright 2011/ELSEVIER

subunits to the complete complex without incorporation of the assembly pathways, assembly intermediates, and spatial heterogeneity of the subunits. Meanwhile, the assembly landscapes have been systematically investigated only for a few cases from the experiments, such as ribosome biogenesis shown in Figure 1(a), and ATP synthase,[36] and RNA polymerase.[12]

Here, we investigate the assembly kinetics of 20 complexes and reduced model of ribosome biogenesis (See Table 1 for the names and functions of total 21 complexes) in the context of our whole-cell model of Syn3A. Complexes' compositions were determined by cross-checking the existing genome/proteome annotation and the homology-based function annotation. The assembly pathways, as series of bimolecular association reactions, of the ribosome,[24] RNAP,[12] and ATP synthase[36] were taken as reported, and of others inferred from interactions between subunits. The pathways for the translocation of membrane proteins in Syn3A are curated as shown in Figure 2. For membrane complexes, we varied the assembly rates, and uncoupled the influence from gene expression by defining the unassembled accumulation of assembly intermediates to investigate the effect from different association rates. We further quantified the result by deriving an analytical formula of the unassembled fraction for a simple dimerization model that is correlated with transcription, translation, and mRNA degradation. Specifically, for ATP synthase, multiple strategies were used to discriminate the formation of dead-end assembly intermediates to improve the assembly efficiency.

We evaluate the results of the WCM of Syn3A augmented by the assembly kinetics of all 21 complexes with the full translocation network of membrane proteins by simulating approximately 100 replicates over the cell cycle. The used spatially homogeneous hybrid stochastic-deterministic algorithms are available in the Lattice Microbes software.[9,37] In doing so we can separate out the timescales for gene expression, membrane insertion, complex assembly, and metabolism. By omitting the explicit evaluation of diffusion and incorporating its average effect into the binding rates, the simulations require about 6 hours to cover the complete cell cycle that can easily run in parallel for 25 cell replicates. The code of augmented Syn3A's WCM is available on Github.

Finally, given the recent success of deep learning algorithms to analyze various biological data sets,[38] and specifically their application to learn low-dimensional representations of the data,[39] we examine the time-dependent variation of the data over the cell cycle from the simulation. The simulated time-dependent quantities contain information about the divergence of cell phenotypes. To investigate how metabolic profiles diverge, we analyzed the metabolomics of simulated cells using a deep learning-based trajectory inference pipeline. Specifically, a deep neural network was used to learn a low-dimensional representation of all 148 time-dependent intracellular metabolite concentrations.[39] Then, these learned embeddings were used to construct a trajectory tree,[40] and each lineage reflects a specific cell population characterized with a distinct pattern of metabolomics. To identify potential drivers of cell divergence, we performed differential analysis of metabolite species and reactions at lineage branching points.

Methods

Hybrid Stochastic/Deterministic Algorithm for WCM of Syn3A

Lattice microbe (LM) was developed to simulate stochastic processes in biological cells using the Chemical Master Equation (CME) and the Reaction Diffusion Master Equation (RDME).[37,41,42] Through a python hook, other algorithms can also be incorporated, including the ordinary differential equation (ODE, for metabolic kinetics)[6,9] and Brownian dynamics (BD, for chromosome dynamics).

In this study, we simulate the kinetics at the whole-cell scale in Syn3A using a spatially homogeneous hybrid stochastic/deterministic algorithm CME-ODE, first published on the yeast's galactose switch model and then applied to Syn3A.[6,9] The genetic information process and the macromolecular complex assembly were simulated in CME, and the metabolism simulated in ODE. See File S1 Section Communication between Genetic Information Process and Metabolism for detailed explanations. The diffusion of particles are not explicitly

simulated in the spatially homogeneous CME. Organization of the chromosome through Brownian dynamics and its interaction with nucleoid associated proteins are not included, but the assembly kinetics of these proteins and DNA replication are simulated.

Total 97 unique and independent cell replicates were sampled to capture the stochasticity of gene expression. As shown by the convergence of produced protein FtsY/0429 in Figure S7(a), both mean and variance stabilize to a plateau with cell replicates larger than 50, confirming that the adequacy of 97 cells for estimating expected behavior.

Genetic Information Processes and Metabolism

As the majority of kinetic parameters remain the same as those used in our previous spatially homogeneous WCM of Syn3A,[6] we discuss only the few relevant modifications made and how the kinetics of complex assembly formation was incorporated into the genetic information and metabolic processes.

In Syn3A, DNA replication initiation occurs by sequential binding of the multi-domain DnaAs to the DNA signature sequences near *Ori* region to start bidirectional replication of the circular genome. Only one round of replication initiation and replication is now allowed as a low *Ori:Ter* ratio of 1.21 was calculated from DNA sequencing experiments (available at NCBI SRA PRJNA1257452). Initiation of DNA replication can begin after 20 or more DnaA proteins (Domain III) are bound to the ssDNA near the origin and following 3 DnaA (Domain IV) binding to the 3 DnaA boxes (each 9 NT) on the dsDNA. The previous constraint of 30 DnaA filament along the ssDNA was reduced after calculating the minimal size of the DNA bubble required to allow the binding of helicase in the replisome complex. Furthermore, the on and off rates of DnaA binding to ssDNA during filament formation obtained from smFRET experiments[43] were modified from the average quantities (1×10^5 to 1.4×10^5 $M^{-1}s^{-1}$) and from (0.55 to 0.42 s^{-1}), respectively, that were measured for genetic constructs with DnaA boxes preceding the ssDNA signatures. We approximated the loading of two replisomes in the ssDNA pocket by binding the representative DNA polymerase III

subunit δ HolA/0044 twice at a fast rate of 10^6 $M^{-1}s^{-1}$ as long as the filament is longer than 20. Then, the replication of the circular genome happened bidirectionally from *Ori* to *Ter*, gene by gene.

As in the previous model, each gene is independently expressed in transcription, and its associated mRNA translated and degraded. The process begins with an irreversible binding step (RNAP to DNA gene, mRNA to ribosome or degradasome, respectively) followed by elongation/(de)polymerization reactions. By explicitly simulating the binding, we can identify the occupancy states of the RNAP, ribosome and degradosome and determine if they are actively processing the mRNA. The kinetics of cotranslational translocation of membrane proteins involving SRP/SR, SecA, YidC and Sec translocon upon production of the target sequence are now explicitly included. The detailed reaction schemes and parameters of the gene expression are provided in File S1 Section Genetic Information Process and Section Translocation Networks in Syn3A. In addition, the parameters were summarized in File S3.

The 175 metabolic reactions that connect 148 intracellular metabolites and 49 extracellular metabolites in the growth media are the same as previously published,[6] except the concentrations of any holocomplexes now depend on the assembly kinetics instead of just the representative subunit (Exact reactions in Figure S1, and the list of related complexes in Table 1). In the previous WCM Syn3A, roughly 15% of the cells died due to depletion of phosphoenolpyruvic acid (pep) and ATP. To assure all cells survive, minor changes to the kinetic parameters in the glycolysis pathway and the activated uptake of (deoxy)nucleosides were first made (See File S1 Section 1.1 Metabolism for detailed explanation. See Table S1 for the comparison of nucleoside import rates. See File S3 for the current set of metabolic parameters). As done previously,[6] the thermodynamic analysis of the kinetic parameters was monitored to assure the correct free energy drop along the glycolysis pathway as shown in Figure S2.

As previously done,[6] the time-dependent surface area was calculated as the sum of the area of transmembrane proteins and membrane lipids assuming symmetric cell division start-

ing with a spherical cell of radius 200 nm obtained from cryo-electron tomograms.[7]

Abundances of Protein Complexes and Involved Protein Subunits

We initialized the macromolecular complexes and the involved protein subunits based on the existing proteomics with the following strategy. A holocomplex refers to a complete, functional macromolecular complex that includes all of its essential subunits or cofactors required for full biological activity. Initial counts of protein holocomplexes (annotated as *Init. Cplx. Cnt*) were estimated by their composition and proteomics counts of the subunits, except the ribosome, whose initial count of 500 was derived from cryo-ET tomograms.[6,7] Proteomics coverage for short transmembrane subunits is often not accurately reported, so the counts of the holocomplex were based only peripheral protein subunits for ABC transporters and ATP synthase. Exceptions also included using the SecY subunit count to represent the Sec translocon, the SMC subunit to SMC-ScpAB, and the EcfT subunit to the ECF module, under the argument that these subunits are the major contributor in both structure and function of the holocomplexes. Complex assembly intermediates were initially assumed to not exist.

Another subsequent question was how to partition the abundances of protein subunits measured in the proteomics study (annotated as *Exp. Ptn Cnt*) into free proteins (annotated as *Init. Free Ptn Cnt*) and proteins already incorporated into complexes (annotated as *Init. Assembled Ptn Cnt*). The number of proteins incorporated into complexes was calculated by multiplying the initial counts of complexes by their stoichiometries, summing across complexes if a protein appeared in multiple complexes. After subtracting the number of proteins incorporated into complexes from the measured proteomic abundances, the remaining counts represented the initial free proteins. If this calculation resulted in negative numbers, these were reset to zero. Thus, the total initial protein count (annotated as *Init. Total Ptn Cnt*) was defined as the sum of the initial free count and the count incorporated into the complexes. See File S2 for detailed partitioning of the initial counts of 455 proteins.

Ribosomal proteins exist both as free precursors and in assembly intermediates, typically less than approximately 5% of the total intact ribosomes.[15] Therefore, we assumed that at least 5% of ribosomal proteins are in a free state. Specifically, for ribosomal proteins with measured proteomics counts lower than 525 (representing 500 proteins incorporated into ribosomes and 25 free), the initial free protein count was set to 25. For proteins with counts greater than 525, the initial free count was calculated as the proteomics count minus 525.

Initial Conditions

In the spatially homogeneous CME-ODE kinetic simulation, which does not account for spatial heterogeneity, the state of the system is described by the time-dependent abundances/quantities of each species.

The computational growth medium and initial concentrations of intracellular metabolites remain the same as in our previous model (see File S2 for exact conditions). We assume that the medium concentrations remain constant throughout the 100-minute cell cycle.

The simulation begins with a single copy of the complete circular chromosome, with no DnaA bound to the *Ori*. Most rRNAs are bound to ribosomal proteins and incorporated into ribosomes; therefore, only two free copies each of 5S, 16S, and 23S rRNAs, derived from each two rRNA-encoding genes, were initialized. A Poisson distribution was used to sample the initial count of each unique mRNA species. The mean abundance of each mRNA that used as the sole parameter of the distribution was calculated as the steady-state abundance under fixed cell growth. As a result, the total initial number of mRNA molecules was approximately 400, which doubled during the cell growth. The initial abundances of proteins and macromolecular complexes were assigned as described in the preceding sections.

Compositions and Assembly Pathways of Protein Complexes

The protein complexes existing in Syn3A were determined by the annotations of the functional protein complexes discussed in previous research on Syn3A.[2,5,6,8,10] The compositions

were determined through the comparative studies of these complexes in other model organisms, and also by the prediction on the structure organization of the protein subunits. The assembly pathways of the holocomplexes, if not reported, were inferred from the deposited subcomplex/intermediate structure and the interactions of the subunits. See File S1 Section Macromolecular Complexes in Syn3A and Assembly Pathways for detailed discussions. The list of macromolecular complexes, their functions and initial counts are listed in Table 1. The detailed compositions and assembly pathways of each complexes are in Table S2 and Table S3.

Table 1: Macromolecular Complexes and their Functions in Syn3A

Location	Name	Function	Init. Cplx. Cnt
Cytoplasm	RNAP	Gene Transcription	93
	Ribosome	Translation/Translocation	500
	SMC-ScpAB	Structural Maintenance of Chromosomes	101
	Gyrase	DNA Gyrase	122
	Topo-IV	DNA Topoisomerase	78
	RNDR	Ribonucleoside-diphosphate reducatese	50
Membrane	Degradosome	mRNA Degradation	120
	Sec Translocon	Translocation	66
	ATP Synthase	Reversible ATP Synthesis	108
	rnsBACD	Import nucleoside	145
	Opp	Import amino acids	241
	PotABC	Import spermine	104
	ThiBPQ	Import thiamine diphospahte	20
	Pst system	Import phosphate ions	123
	ribflECF	Import riboflavin	10
	p5pECF	Import pyridoxal phosphate	10
	5fthfECF	Import 5-Formyltetrahydrofolate	10
	nacECF	Import Nicotinate	150
	coaECF	Import Coenzyme A	10
	KtrCD	Import K^+	38
	Fak	Phosphorylation of Fatty Acid	206

Assembly Rate of Protein Complexes

Under the spatially homogeneous assumption in CME kinetics, a lumped association reaction of two particles to form a complex (A+B to C) contains first the relative diffusion between two particles and then the intermolecular interactions to overcome the barrier to form a stable complex.[33]

One association is diffusion-controlled when the rate of binding is limited by the rate at which the proteins diffuse through the medium to encounter each other, rather than by the intrinsic reaction kinetics of binding. Without considering steric specificity, the Smoluchowski equation ($k_D = 4\pi DR$, where D is the relative diffusion coefficient and equals $D_1 + D_2$, R is the contact distance between the centers of the two spheres) gave a binding rate on the order of 10^7 $\mathrm{M^{-1}s^{-1}}$ between 3D diffusive cytoplasmic proteins. Considering the steric specificity of the proteins, the diffusion-controlled association rates were estimated between 10^4 and 10^6 $\mathrm{M^{-1}s^{-1}}$.[32] Here, we adopted the association rate for cytoplasmic complexes, $k^{\mathrm{cyto}}_{\mathrm{assembly}}$ of 10^5 $\mathrm{M^{-1}s^{-1}}$.

The association of protein subunits can be significantly altered by their localization. Transmembrane proteins diffuse one to two magnitudes slower in confined 2D membrane than cytoplasmic proteins. For example, diffusion coefficient of 0.02 $\mu\mathrm{m^2s^{-1}}$ was observed for the transmembrane protein LacSΔIIA-GFP in Gram-positive *Lactococcus lactis*, and a much faster coefficient of 7 $\mu\mathrm{m^2s^{-1}}$ for its counterpart cytoplasmic protein GFP[44]). However, the pre-orientation of reactive regions and the longer lifetime of the transient complex largely compensate for the reduced diffusion coefficient.[19,45] The same logic applies to the peripheral membrane proteins that slide on the membrane. Based on these arguments, we tested here three values for the membrane association rates of 10^5, 10^4, and 10^3 $\mathrm{M^{-1}s^{-1}}$ for $k^{\mathrm{mem}}_{\mathrm{assembly}}$, for the binding between peripheral membrane subunit and transmembrane subunits, and between two transmembrane subunits.

Construction of Protein Translocation Network

To clarify the three translocation pathways in Syn3A shown in Figure 2, the related entities were summarized in Table 2. The total number of ribosomes was estimated from cryo-electron tomograms of a cell with a radius of 200 nm;[7] the abundances of proteins (subunits) came from our proteomics study using quantitative mass spectrometry.[2]

The SecYEGDF translocation machinery (bacterial SecY family member[30] with auxiliary SecDF subunit,[46] hereafter Sec translocon) and YidC insertase (bacterial Oxa1 family member[30]) are responsible for the insertion of transmembrane proteins and secretory proteins. YidC insertase, independent of the Sec translocon, could promote the insertion of a subset of TMPs with short translocated regions,[30] as well as functioning in conjunction with the core Sec translocase to assist the insertion of long translocated regions into the membrane.

The signal recognition particle (SRP, consisting of protein Ffh/0360 and 4.5S non-coding RNA from gene 0049) and the signal receptor (SR, FtsY/0429) mediate the cotranslational translocation of transmembrane proteins. SecA/0095 was previously known to insert secretory protein across the membrane in concert with the SecB chaperon and the Sec translocon,[47] yet recent selective ribosome profiling proved its role in cotranslational recognition and insertion without chaperons.[48] It should be noted that the count of SRP is almost the same as ribosomes, while in *E. coli*, the number of ribosomes largely exceeds SRP and SecA by up to two orders of magnitude. This could lead to the loss of SRP targeting specificity, as verified by selective ribosome profiling experiments in *E. coli* when overexpressed SRP bound to cytoplasmic, periplasmic, and outer membrane proteins.[49] In Syn3A, this reduced substrate specificity could presumably decrease the efficiency of translocation of transmembrane proteins with unnecessary Sec translocon occupation. Without measurement of RNC/SRP interactome from selective ribosome profiling, here we assume that SRP can only target transmembrane proteins.

Two lipoprotein modifiers, lipoprotein diacylglyceryl transferase (Lgt/0818 and Lgt/0820, EC 2.5.1.145) and lipoprotein signal peptidase (SPaseII, LspA/0518, EC 3.4.23.36, PDB

entry 5DIR) were found in Syn3A. Due to the minimized genome, Syn3A only possesses DnaK/DnaJ/GrpE and ClpB chaperon systems for protein folding and disaggregation, respectively. Two transmembrane proteases, FtsH/0039 and YqgP-GplG/0516, and one cytoplasmic protease Lon/0394 degrade proteins to peptides, and five peptidases further decompose them into amino acids to prevent protein aggregates and to recycle amino acids.

Table 2: Abundances of Macromolecules in Syn3A's Translation/Translocation Network [a]

Category	Translocation Entities	Absolute Count	Localization[b]	Ess.[c]
Ribosome	Total Ribosome	500	CP	E
SRP	Ffh/0360	365	CP	E
	4.5S RNA/0049	-	CP	E
SR	FtsY/0429	88	PMP	E
SecA	SecA/0095	573	CP	E
Sec Translocon	SecY/0652	66	TMP	E
	SecE/0839	8	TMP	E
	SecG/0774	4	TMP	Q
	SecDF/0412	215	TMP	E
YidC	YidC/0908	120	TMP	E
Lipoprotein Modifier	Lgt/0820, 0818	13	TMP	E
	LspA/0518	3	TMP	E
Proteases	Lon/0394	757	CP	Q
	FtsH/0039	148	TMP	E
	YqgP-GplG/0516[5]	63	TMP	Q

[a] Absolute Counts in the initial of the simulation
[b] CP: Cytoplasmic protein, PMP: Peripheral membrane protein, TMP: Transmembrane protein
[c] Ess.: Essentiality, E: Essential, Q: Quasiessential, N: Nonessential

Three curated translocation pathways summarized in Figure 2 are, the cotranslational SRP/SR/Sec and SecA/Sec pathways and the post-translational sole YidC pathway. Substrate proteins of different translocation pathways were determined with bioinformatic predictions, together with gene functional annotations.

In the SRP/SR/Sec pathway, translation starts from mRNA diffusing and binding to a ribosome, forming the ribosome nascent chain complex (RNC), and the elongation of the

polypeptide chain will expose the targeting sequences. For the SRP/SR/Sec pathway, SRP can diffuse and recognize the RNC to form a SRP_RNC complex. Since bacterial SRPs do not have an additional Alu domain to arrest translation elongation, the polypeptide chain is allowed to grow with normal speed.[49] The binding of SRP to SR occurs through the interactions of each GTPase domain near the peripheral membrane and is fast enough with k_{on}=10^7 M^{-1} s^{-1} with SRP when loaded with RNC.[50] The cytosolic loops of the Sec translocon could interact the A domain of FtsY and the ribosomal protein L23 at the nascent polypeptide exit site, thus facilitating the effective formation of the quaternary complex with K_d=2 μM.[51] The Sec translocon activates the GTP hydrolysis of SRP_SR targeting complex and the handover of RNC cargo to the Sec translocon channel at a rate of 0.95 s^{-1}.[51] The last step is the elongation and translocation, and the translation elongation serves as the driving force in inserting the polypeptide chain into the membrane. The rate of insertion and folding of transmembrane proteins was estimated to be above 20 aa/s based on one *in vitro* study on protein lactose permease inserted by SecYEG and YidC,[52] while the chain elongation speed was 12 aa/s, thus the translation elongation is the rate-determining step, and the overall rate of elongation and translocation was depicted by the Hofmeyr rate law.

YidC and Sec translocon collaborate to insert different parts of membrane proteins, where YidC is responsible for short hydrophilic segments and Sec translocon for long hydrophilic segments.[30] The copurification experiment indicated that YidC binds to the Sec translocon by interacting with the SecDF subunit.[53] Here, it was assumed that YidC will only associate with the RNC_Sec translocon complex transiently via its interaction with SecDF to finish the insertion, after which it will disassociate from the Sec translocon.

The failure of cotranslational targeting occurs when the emerging polypeptide chain grows too long, weakening the interaction between the ribosome and SRP. According to selective ribosome profiling, the length of the nascent polypeptide chain lies between 50 and 100 residues when SRP binds to RNC.[49,54] Here we use the metric of the length of polypeptide chain shorter than 100 AAs before the SRP recognition. In this case, the degradation of

the protein presumably occurs to prevent the protein aggregates and to recycle amino acids. From the mutant experiments of two proteases, Lon and FtsH in *Mycoplasma pneumoniae*,[55] membrane proteins are the main targets for the transmembrane protease FtsH. Considering the transmembrane region in the nascent polypeptide chain as the hydrophobic signal target, here it was assumed that the degradation of the unsuccessfully translocated transmembrane protein occurs through its binding to FtsH, supported by the *in vitro* degradation of SecY by FtsH.[56] The degradation kinetics and the cost of ATP depend on the stability of the protein substrate and the hydrolysis rates of ATP.[57] Here we take the maximum degradation rate 0.22 min^{-1}. The further decomposition from the peptide to amino acids by peptidase is approximated to be combined within this reaction. We assume that ATP energizes the degradation with one ATP per amino acid and that the entire protein is digested.

In the sole YidC pathway, YidC could function separately from Sec translocon on transmembrane proteins with only short hydrophilic translocated segments.[30] Tail-anchored membrane proteins (TA) with one or two transmembrane regions (TMRs) and the targeting TMR located less than 65 amino acids from the C-terminus are post-translationally translocated by YidC, since the short amino acid distance leaves no time for cargo transfer to the Sec translocon.[29] In this pathway, cotranslational recognition of TMR by SRP is unnecessary, and after translation is completed, TAs could diffuse to the inner membrane and bind to YidC. Binding with YidC will assist in inserting a short TMR into the membrane without the Sec translocon. The rate at which YidC inserts TA proteins into the membrane was set at 1 s^{-1} under the argument that YidC incorporated only the short TMR of 20 AAs in the lipid membrane and the rate of insertion was faster than 20 aa/s.[52]

Translocation of secretory proteins could occur through both cotranslational and post-translational pathways.[58] In Syn3A, the previously well-recognized post-translational translocation pathway of secretory proteins[47] is less likely. The translocation-competent state of the nascent polypeptide chain is required before/during the targeting and insertion, and this state is usually maintained by SecB chaperon which has been characterized in *E. coli*.[58]

Since SecB is not in Syn3A, and there is no direct evidence showing that existing chaperon systems DnaK/DnaJ/GrpE and ClpB or SecA could compensate for SecB's role, therefore the translocation of translated nascent chain would not succeed.

The targeting factors for secretory proteins could be SRP/SR (more recognized for TMPs and preferring a high hydrophobic signal peptide) or SecA (more recognized for secretory proteins). With no measurement of the RNC interactome with SRP and SecA from selective ribosome profiling to know the discrimination of substrates for SRP/SR and SecA, it was assumed here that the translocation of secretory proteins is facilitated by only SecA. Another factor that favors the cotranslational pathway is the absence of the trigger factor (TF), which hinders and delays SecA engagement, leading to post-translational translocation.[48,59]

In cotranslational translocation via SecA/SecC, SecA first recognizes the signal peptide emerging from the ribosome exit tunnel and directs the binding to the Sec translocon. In this fashion, protein misfolding is prevented and translocation is rapid. SecA selective ribosome profiling revealed that the length of the nascent polypeptide chain lies between 100 and 150 residues when SecA binds to RNC,[48] and here the recognition failure by SecA, similar to SRP, was also considered using the metric of 150 residues. However, lipoproteins 0481, 0605, and 0851 are of lengths 145, 102, and 68 AAs, thus we roughly assumed thresholds of half the protein lengths. SecA ATPase inserts the secreted polypeptide chain across the membrane under ATP hydrolysis, which is also enhanced by SecDF using the proton motive force.[46] Protein SecDF/0412 is a transmembrane protein with 12 TMRs and a large extracellular domain P1. As an auxiliary factor, SecDF is believed to be incorporated in insertion late after SecA, when its P1 domain binds to the unfolded protein on the outer leaflet membrane surface and pulling the chain out with repeated conformational transitions driven by the proton gradient.[60] Here, it was assumed that the insertion by SecA and the pull by SecDF were much faster than the elongation of the polypeptide chain, and the Hofmeyer rate law was used to depict the rate of cotranslational translocation.

Modification of lipoproteins occurs upon translocation with Lgt and Lsp for proper func-

tion. Lgt transfers the diacylglyceryl group from phosphatidylglycerol (PG) to the sulfhydryl group of the cysteine residue in the lipobox, and then Lsp cleaves the signal peptide up to the cysteine residue, leaving an exposed α-amino group of diacylglyceryl-systeine.[61] Mature lipoproteins anchor to the outer leaflet of the membrane by embedding the lipid-modified cysteine residue[62] in Figure 2.

Extracellular proteins are also cotranslationally translocated across the membrane. However, without signal peptidase (SPase I) identified, it is assumed that the translocated proteins are released to extracellular media without signal peptide cleavage.

Proteins without signal peptides or transmembrane regions are translated in the cytoplasm. They could be further categorized into peripheral membrane proteins and cytoplasmic proteins. Peripheral membrane proteins could reversibly diffuse back/forth between the cytoplasm and the peripheral membrane region until they are trapped by specific and strong interactions, such as forming a complex with TMPs, The diffusive behavior on the membrane is generally constrained 2D sliding under nonspecific hydrophobic interactions with membrane lipids.[19] The proteins in the cytoplasm are translated and then function in the cytoplasm. Under the spatially homogeneous assumption, no explicit diffusion was simulated, and instead, reversible exchange reactions of peripheral membrane proteins were implemented between the cytoplasm and the peripheral region to account for their spatial distribution.

The translocation pathways and diffusive behaviors of protein in different localization were summarized in Table S7. The implemented reactions of the preceding behaviors are summarized in Table S8.

Revision of Protein Localization, and Identification of Targeting Sequences for Translocation

Targeting sequences were determined with the new prediction of two bioinformatics tools, Signal P 6.0[63] and DeepTMHMM.[64] SignalP 6.0, a machine learning-based tool, was used

to identify signal peptides, short amino acid sequences that direct proteins to secretory pathways and are cleaved by signal peptidase (SPase) after translocation. In addition, it could differentiate the signal peptide for SPase, SPase I for Sec SPs in extracellular proteins, and SPase II for lipoprotein SPs in lipoproteins.[58] DeepTMHMM was used to predict the locations of different protein segments, including the signal peptide and extracellular part of secretory proteins and the TMRs of transmembrane proteins. The prediction of signal peptides from DeepTMHMM was compared with that from SignalP to further verify our localization assignment of secretory proteins. The structural organization of TMRs determined the topology of transmembrane proteins, i.e. the positions and lengths of TMRs, and also intracellular and extracellular loops and their orientations, which affect the translocation mechanism. SignalP 6.0 and DeepTMHMM are available online. When performing SingalP 6.0, we chose Organism as other for bacteria, and Model as slow for accurate region borders of the targeting sequences.

Minor revision of protein localization from the previous publication were made.[2,6] A total of 455 proteins (subunits) are localized in four regions, 315 in the cytoplasm, 38 in the peripheral membrane, 84 in the transmembrane, 15 as secretory proteins, with 3 proteins left unidentified shown as pie chart in Figure S6.

The signal peptides predicted by SignalP all originate from the N-terminus and range in length from 15 to 28 residues. Transmembrane regions (TMRs), which serve as targeting sequences for transmembrane proteins (excluding tail-anchored proteins), typically begin within the first few to 50 residues from the N-terminus and span approximately 10 to 20 residues in length. See File S2 for the function, localization, signal peptide, and topology of each proteins. See Table S6 for the full list of tail-anchored membrane proteins.

Machine Learning-Based Trajectory Inference for Metabolic Profile

To investigate how cells evolve into different metabolic phenotypes, we analyzed metabolic profiles using a three-step trajectory inference pipeline. First, we trained a deep neural net-

work on the raw metabolite data to obtain a low-dimensional representation. The raw data set comprised 148 unique intracellular metabolites, collected at 6,000 time points, for each of the 97 cell replicates. Then we built a trajectory tree using this representation, where different lineages diverge from the same root/origin (due to the same initial concentrations) over time. Each lineage represents a different cell population, and we classified cells by projecting each cell's trajectory onto every lineage, summing the path-to-lineage distances, and assigning the cell to the lineage with the smallest total distance. Finally, at the points where the lineages diverged, we identified metabolite species and reactions that are significantly different between emerging cell populations.

Representation Learning via Autoencoder

In the first step, we applied an autoencoder to compress raw metabolite concentrations into low-dimensional representations. An autoencoder is a powerful tool in unsupervised representation learning[39,65,66] and has been widely applied in biological data analysis.[67,68] It consists of an encoder and a decoder. The encoder enables the compression of high-dimensional data into a low-dimensional representation, and the representation is optimized by reconstructing the original data via a decoder. This structure allows the model to preserve all essential signals in the representation while removing noise.

The metabolite concentrations recorded every second throughout a complete cell cycle are used as input for the autoencoder. In total, there are 148 intracellular species. The number of recorded time points varies between cells depending on the cell cycle duration, ranging from 93 to 110 minutes. The encoder is a fully connected three-layer network containing 64, 32 and 16 neurons, respectively. ReLU activation that takes the nonnegative part of its argument is used to introduce nonlinearity. The output of the final encoder layer serves as the compressed and learned representation of the input concentrations traces and is used in trajectory tree construction. The decoder mirrors the encoder's structure, with an output layer matching the dimensionality of the input data. The optimal model is determined by

minimizing the following loss function $\mathcal{L}$:

$$\mathcal{L} = \frac{1}{NT} \sum_{i=1}^{N} \sum_{t=1}^{T_i} \left\| X_{i,t} - \hat{X}_{i,t} \right\|^2 + \lambda \| C - I \|$$

where N is 97 as the number of cell replicates, T is the summation of length of time points of all N cell replicates, T_i is the length of time points for cell i, $X_{i,t}$ denotes the metabolite concentrations of cell i at time t, $\hat{X}_{i,t}$ represents the reconstructed metabolite concentrations, C is the covariance matrix of latent factors, and I is the identity matrix, λ is the regularization coefficient. The first term quantifies the reconstruction loss, ensuring that the learned representation retains as much information from the original data as possible. The second term is a regularization term that decorrelates the different dimensions of the representations to prevent them from capturing redundant information.[69,70] The hyperparameter λ balances the weights of the loss of reconstruction and the regularization term. In practice, we select the value of λ to be 3 by grid search over a range of values.

Trajectory Tree Construction and Cell Classification

In the second step, we constructed a trajectory tree with the learned representations using Slingshot.[71] Slingshot is a lineage inference tool with two stages:

1. Identify global lineage structures by constructing a minimal spanning tree (MST) on clustered data points. Here we clustered the data points using the k-means algorithm. We determined the optimal number of clusters through the grid search and selected the value that allows the initial trajectory tree to capture the growth dynamics of the cells more effectively. The optimal number of clusters was found to be 9.

2. Refine each lineage using principal curves and estimate pseudo-time variables for cells along each lineage. The pseudo-time variable represents the growth stage of the cell along the lineage.

Each lineage on the tree represents the metabolite profile of a distinct cell population. Cells are assigned to the population that has the smallest distance to their trajectory path.

Between-Lineage Differential Analysis

After cells are clustered into distinct populations, the next key question is to identify which metabolite species or reactions drive cell divergence. To address this, we performed a differential analysis between each pair of lineages. First, we define the branching point as the time at which the distance between the two lines exceeded a predefined threshold ϵ, indicating the starting point when cells start to diverge into different types. To identify hidden biological changes related to cell divergence, we compared metabolite concentrations and reaction fluxes at the branching point between different cell types. Two-sample t-tests are used to each metabolite and reaction to determine whether their differences between lineages are statistically significant. To adjust for multiple hypothesis testing and control false discovery rate, the Benjamini-Hochberg procedure is applied to adjust the p-values,[72] and we considered a metabolite species or reaction significantly different if its adjusted p-value fell below significance level $\alpha = 0.05$. We then quantified the magnitude of these differences using standard effect sizes (Cohen's d statistic). Cohen's d is calculated as the difference between the two group means divided by the pooled standard deviation, and the large Cohen's d means a significant difference between the group means.

We also reported the separation time between each pair of lineages. To calculate this, we projected the cell trajectories that pass through these two lineages onto the tree and identified the time when each cell crossed the branching point. The separation time for this lineage pair was defined as the average of these times.

Results and Discussion

Ribosome biogenesis under the constraint of subunit synthesis with the reduced SSU assembly pathway

Downstream of gene expression, the formation of macromolecular complex is constrained by subunit synthesis where proteins are translated from mRNA and three rRNAs in ribosomes are the direct transcription products. Assembly intermediates generated along various pathways can accumulate and reduce assembly efficiency for two main reasons in the context of the time-dependent whole-cell model. First, bottleneck subunits—those with the lowest available counts—limit the maximal possible amount of assembled complex and lead to the buildup of upstream intermediates. Second, the assembly process entails waiting periods necessary for the sequential binding of subunits to intermediates via bimolecular reactions. To quantify the impact of the second reason, we calculated the unassembled accumulation by subtracting the count of assembled holocomplexes from that of the bottleneck subunit. This value represents intermediates that are capable of progressing to fully assembled complexes but remain incomplete due to delays in bimolecular binding.

Ribosome biogenesis from 3 rRNAs and nearly 50 ribosome proteins using the reduced SSU assembly pathway in Figure 1(a) nearly duplicated the initial 500 ribosomes with a median of 400 assembled at the end of the cell cycle (distribution in Figure S7(f)). SSU and LSU were assembled at consistent paces with nearly parallel trajectories shown in Figure 3(a). While the formation of SSU was faster than LSU, a surplus up to 80 of SSU occurred at the end of the cell cycle. To reason the differences of assembly between SSU and LSU, the bottleneck subunits of SSU, LSU, and the entire ribosome were identified in Figure 3(b). For SSU, ribosomal proteins S5, S16, and S4 as the binders to 16S rRNA 5' domain mainly limits the assembly of SSU. For LSU, 23S rRNA (in more than half of the cells) as the starting point of assembly, limits the formation of LSU. The next bottleneck subunit is 5S rRNA, which associates with the LSU as the 17th of 32 total binders, and up to 10 copies of the

intermediate that binds 5S rRNA were observed to accumulate. The bottleneck subunits for LSU and ribosome were nearly identical, disclosing that the synthesis of subunits for LSU constrained the formation of ribosome, which explains the neat accumulation of SSU.

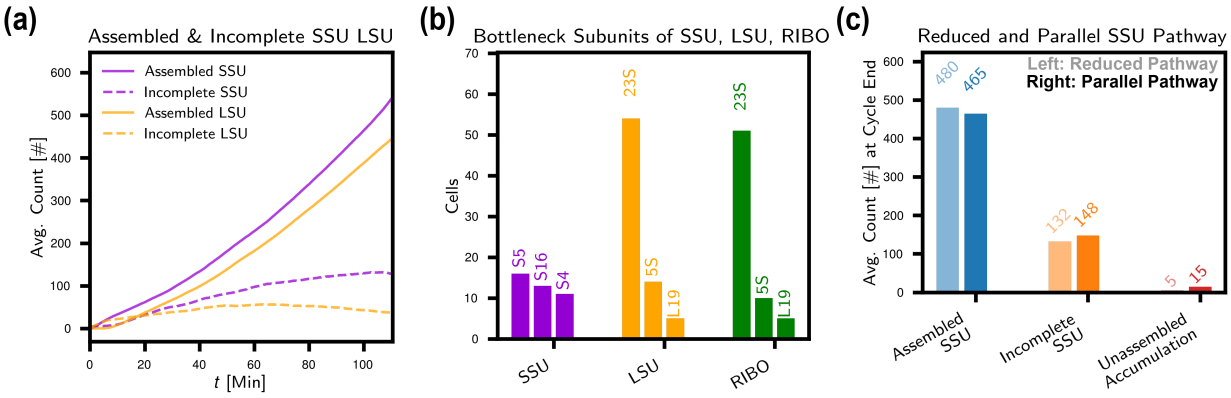

Figure 3: Ribosome biogenesis under the constraint of subunit synthesis with the reduced SSU assembly pathway. (a) Assembled and incomplete ribosome SSU and LSU with the reduced SSU assembly pathway. (b) Top three bottleneck subunits for ribosome SSU, ribosome LSU, and ribosome at the end of cell cycle. (c) Assembled SSU, incomplete SSU, and unassembled accumulation of SSU at the end of cell cycle with parallel or reduced SSU assembly pathways.

Assembly intermediates (calculated as the summation of intermediate counts from bare rRNA to the last intermediate) accumulated over time for both the SSU and LSU, as shown in Figure 3(a). Both the bottleneck subunits that stall assembly midway and the waiting times required for sequential bimolecular binding events can contribute to the accumulation. The quantified unassembled accumulation was 5 for SSU assembly with the reduced pathway, while the average abundance of SSU intermediates were up to 130. As shown in Figure 3(b), for SSU the bottleneck effect came from ribosomal proteins, which means that the assembly of SSU was stuck in the middle more due to the lack of proteins. In contrast to SSU, the synthesis of 23S rRNA dominantly restricts the LSU assembly, thus the incomplete LSU was less trapped. Meanwhile, due to the longer assembly pathway, unassembled accumulation played a larger role for LSU and occupied 20 out of the 40 accumulation of intermediates. As another support of this, the assembled LSU started to emerge around 5 to 10 min, later than the SSU around 2 min since 31 LSU ribosome proteins and 5S rRNA must bind to 23S

rRNA, while only 20 SSU ribosome proteins bind to 16S rRNA.

To quantify the impact of reducing the SSU assembly pathway from a parallel network of 145 intermediates to a nearly linear sequence of 19 intermediates, we compared the incomplete SSU and unassembled accumulation under two conditions, as shown in Figure 3(c). (A separate set of 50 cell replicates was sampled.) When transitioning from the highly parallel to the reduced pathway, the number of SSU intermediates decreased from 148 to 132, and the unassembled accumulation dropped from 15 to 5. This reduction is attributed to the narrower distribution of the 19 intermediates, suggesting that the linear pathway yields a slight improvement in assembly efficiency. However, as noted previously, parallel assembly pathways provide additional redundancy under stress conditions—such as rRNA misfolding.[13] Since the current model does not account for cellular perturbations, the simplified linear pathway serves as a reasonable approximation. Over the course of the entire cell cycle, the total number of assembled SSUs reached 500, making the difference in unassembled accumulation relatively minor by comparison.

Dependence of complex formation upon rate of assembly

The assembly rates of many protein complexes remain poorly characterized, particularly for membrane-associated complexes. Furthermore, it is unclear how these assembly rates influence the overall rate of complex formation and the abundance of fully assembled structures, especially given the time scales associated with subunit synthesis. To investigate this relationship, we varied the bimolecular assembly rates of membrane subunits for membrane-associated complexes from 10^5 M^{-1} s^{-1} to 10^4 and 10^3 M^{-1} s^{-1}.

Here, we used the assembly of rnsBACD, the nucleoside ABC transporter as an example. Before the assembly of subunits, the translocation of subunits of membrane complexes occurs through the pathways in Figure 2. The two transmembrane subunits RnsD/0008 and RnsC/0009 as TMDs of rnsBACD are translocated via the SRP/SR/Sec pathway. The peripheral membrane ATP binding subunit RnsA/0010 as NBD is translated in the cyto-

plasm, and the substrate binding domain (SBP), lipoprotein RnsB/0011, is translocated via SecA/Sec pathway then undergoes modification by Lgt and Lsp. Upon translation and translocation of four subunits, the assembly assumably starts with two TMDs (RnsD/0008 and RnsC/0009) binding to form the permease channel. Then, the ATP binding domains (RnsA/0010) and substrate binding protein (SBP, RnsB/0011) associate with the channel. The initial count of the rnsBACD holocomplex was set to 145, same as the proteomics abundance of the peripheral membrane protein RnsA/0010. The initial counts of free RnsD, RnsC, RnsA, and RnsB are 0, 30, 0, and 0 respectively.

The unassembled accumulation of rnsBACD intermediates increased significantly with the slower assembly rate as shown in Figure 4(a). At the higher assembly rate of 10^5 M^{-1} s^{-1}, unassembled accumulation was few and minor during the cell cycle, and the highest count of the holocomplex rnsBACD (101 of 145, 70% of the initial count) were assembled at the end of the cell cycle in Figure 4(b). Subunit RnsB/0011 late in the assembly pathway had a increase with decreasing assembly rate as to be expected in Figure 4(c). The variation in the numbers of the different intermediates and subunits demonstrates the complexity of the assembly landscapes.

The correlation between decreased assembly yield and slower assembly rate occurred for most of the 14 membrane complexes to different extents Figure 4(d). The fact that the scaled abundance for none of the holocomplexes was doubled at the end of the cell cycle, emphasizes the need for the fast association rate of membrane proteins. This result can be rationalized by considering the formation of a binary holocomplex given the kinetic parameters for the coupled transcription, translation, and mRNA degradation in gene expression. The evaluated unassembled fraction ϕ, defined as the ratio of unassembled protein over the total synthesized protein at the end of the cell cycle, t_{cycle} was in Equation 2. N_A is the Avogadro constant, V_{cell} the cell volume, $N_{Ava,RNAP}$, $N_{Ava,Ribo}$, and $N_{Ava,Degra}$ the count of free/available RNAP, ribosome, and degradosome, N_{gene} the count of the protein-encoding gene, $k_{bind}^{gene:RNAP}$, $k_{bind}^{mRNA:Ribo}$, and $k_{bind}^{mRNA:Deg}$ the binding rate in transcription, translation

and degradation reaction, $k_{assembly}$ is the protein assembly rate. ϕ increased from only 1.3% to 13% when $k_{assembly}$ slowed from 10^5 to 10^3 M^{-1} s^{-1}. The decreased efficiency will propagate along the assembly pathways and further suppress the yield of the final holocomplex, especially for long pathways, such as ATP synthase in Figure 4(d). Here, using the quantified unassembled fraction, we argue that the binding rate should be equal or larger than 10^5 M^{-1} s^{-1} to alleviate the unassembled accumulation of assembly intermediates in the context of the coupled subunit synthesis from gene expression.

$$\phi = \frac{\text{Not Assembled}}{\text{Total Synthesized}} \tag{1}$$

$$= \frac{N_A V_{cell}}{t_{cycle}} \sqrt{\frac{N_{Ava,Degra} k_{degra}^{bind}}{N_{Gene} N_{Ava,RNAP} k_{bind}^{gene:RNAP} N_{Ava,Ribo} k_{bind}^{mRNA:Ribo}} \frac{1}{k_{assembly}}} \tag{2}$$

With the present kinetic parameters for genetic information processing, the abundances of the membrane complexes do not double over the cell cycle even with the fastest assembly rate in Figure 4(e). The primary reason is the constraint imposed by insufficient—and more importantly, non-stoichiometric—subunit synthesis from gene expression, as further discussed for ATP synthase in the following section.

Assembly of ATP synthase highlights the co-expression of subunits and the alleviation of undesired structures

An important example for the stoichiometric balance of subunits, ATP synthase has eight distinct subunits that possess different stoichiometries of 1 (subunit ϵ, γ, δ, and a), 2 (subunit b), 3 (subunit β, and α), or 10 (subunit c)[73] to a complete structure of $\alpha_3\beta_3\gamma\epsilon\delta c_{10}ab_2$. In our simulations, the initial count of intact ATP synthase was given as the number of peripheral F_1 subunit ϵ (108) considering the stoichiometric ratio among the F_1 sector subunits α, β, γ, and ϵ (See Table S2). To approximate the stoichiometric balance of subunit synthesis, our current

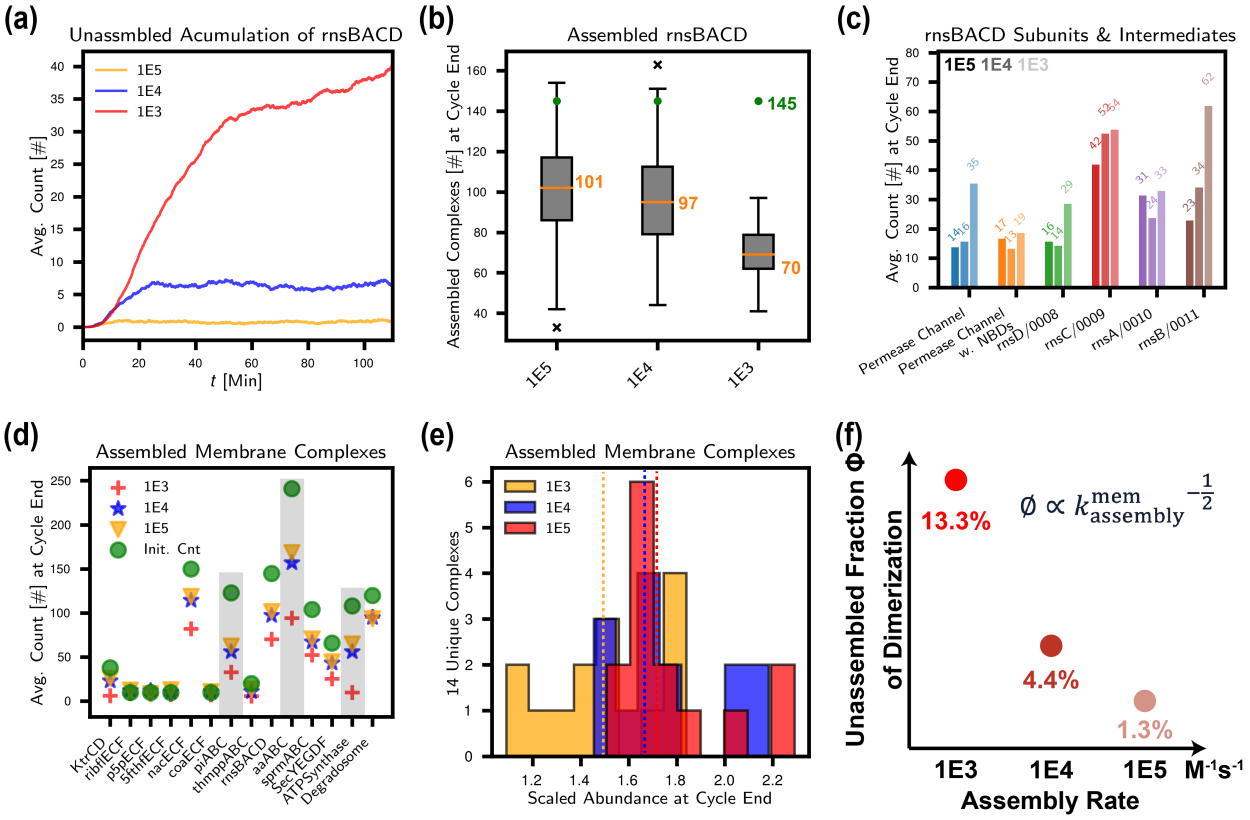

Figure 4: Assembly rate needs to match up with subunits synthesis speed from gene expression. (a) Unassembled accumulation of rnsBACD assembly under 10^5, 10^4, and 10^3 $M^{-1}s^{-1}$ assembly rate. (b) Distribution of assembled rnsBACD among population under 10^5, 10^4, and 10^3 $M^{-1}s^{-1}$ assembly rate. Initial count of complex is 145 shown as green dots. (c) Counts of rnsBACD assembly intermediates and subunits under 10^5, 10^4, and 10^3 $M^{-1}s^{-1}$ assembly rate at the end of the cell cycle. (d) Comparison of population averaged assembled membrane complexes under 10^5, 10^4, and 10^3 $M^{-1}s^{-1}$ assembly rate. (e) Distribution of population averaged scaled assembled membrane complexes under 10^5, 10^4, and 10^3 $M^{-1}s^{-1}$ assembly rate with median of 1.70, 1.66, and 1.5, respectively. (f) Unassembled fraction scales proportional to the reverse of root of assembly rate in a one step dimerization reaction hooked with gene expression of two subunits.

implementation differentiated promoter strength at transcription level by linearly scaling the promoter strength with the subunit abundances. With this strategy, the synthesized mRNA (relative to ϵ/0789) has a rather linear relationship with the stoichiometries (ϵ 1/1, β 3/2.7, γ 1/1.1, α 3/2.5, δ 1/1, b 2/1.9, c 10/6.8, and a 1/0.87). However, experimentally obtained mRNA abundances show a larger deviation from the stoichiometries for subunit δ, b, c, and a as 1/0.5, 2/1.4, 10/4.3, and 1/1.9, respectively. The experimental abundances were derived from short-read RNA sequencing experiments.[4] A similar deviation has also been observed in long-read RNA sequencing experiments in a synthetic relative to Syn3A, Syn1.0 (data unpublished). The inconsistency between the mRNA abundances and the stoichiometries for our WCM simulations and those observed experimentally is attributed to our implementation of gene expression in the model. mRNA processing, mRNA stability, differential transcription, and differential translation have been well characterized to impact mRNA (and protein) expression levels,[74] however without the experimental detail to capture these processes accurately we simplified and assumed a linear link (proxy promoter) between protein and mRNA expression to ensure stoichiometric expression within complexes.

In general the stoichiometric balance of the eight subunits was roughly maintained on average as shown in Figure 5(a), where the synthesized subunits over their corresponding stoichiometries ranged from 100 to 130 at the end of the cell cycle. However, 65 intact ATP synthase (60% of the initial 108) on average were assembled at the end of the cell cycle, significantly less than the median of the synthesized subunits. We reason the inconsistency between synthesized subunits and assembled complete ATP synthase from two aspects. First, the strong heterogeneity of subunit synthesis at single-cell level exists and undermines the efficiency of assembly by the non-stoichiometric expression of the eight subunits. The quantified coefficient of variances (CVs) of synthesized subunits over the stoichiometries for each cell replicate were moderate with a median of 0.3. Thus, the surplus of certain precursors and the accumulation of intermediates occurred differently in each cell but could not be assembled into the holocomplex, then causing the waste of assembly building blocks. At the

end of the cell cycle, the highest possible counts of ATP synthase (i.e. the lowest count of subunits over stoichiometries) had a mean of 77 and maximum of 109. This subtle point highlights the importance of co-expression of proteins by the polycistronic transcript from the ATP synthase operon.

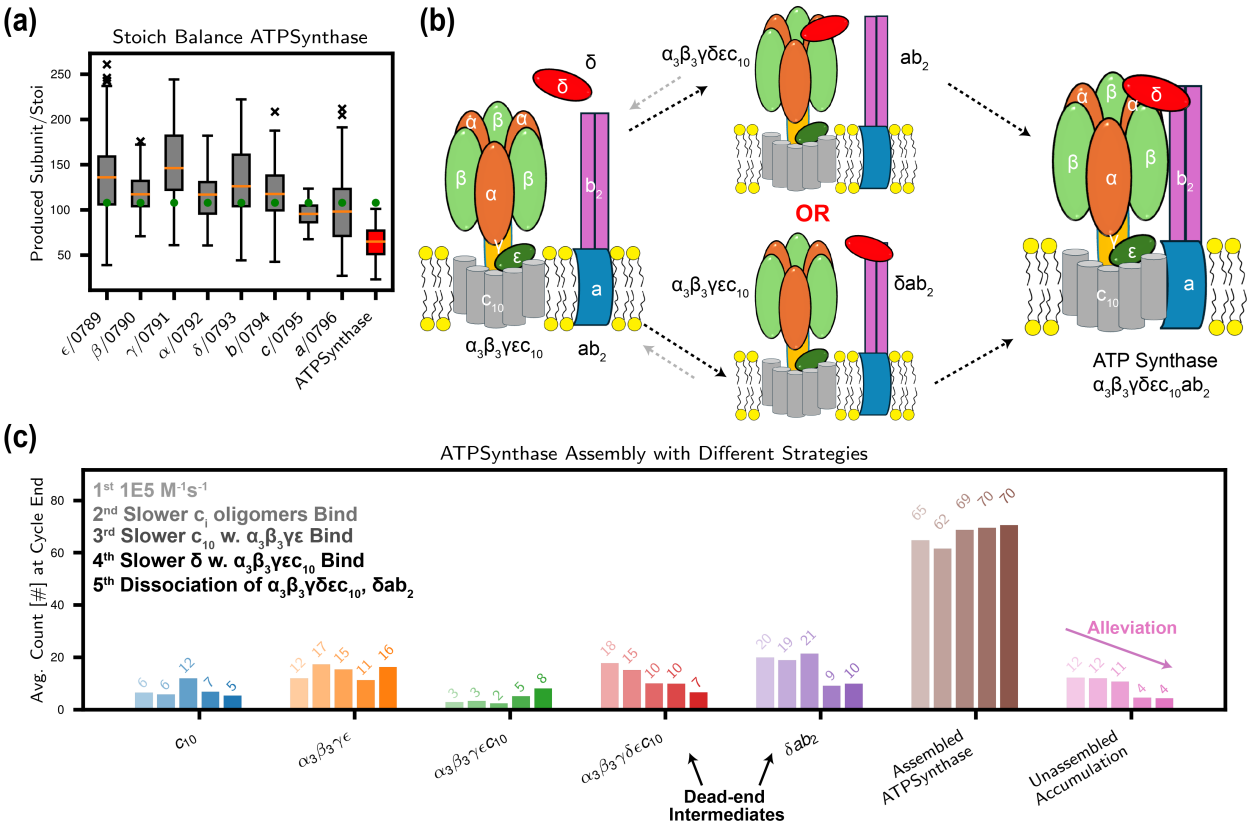

Figure 5: Assembly of ATP synthase. (a) Distribution of synthesized ATP synthase's eight subunits over stoichiometries at the end of cell cycle, and assembled ATP synthase. The green dots denote the initial 108 complete ATP synthases. (b) The last stage association of ab_2 and $\alpha_3\beta_3\gamma\epsilon\delta c_{10}$ to ATP synthase occurs via the glue of δ subunit. However, no direct evidence was reported on the exact mechanism of this process. (c) Counts of intermediates that not incorporated into ATP synthase, assembled complete ATP synthase, and unassembled accumulation under five different assembly landscapes at the end of the cell cycle.

Complexity of the assembly pathway seen in this study is also a factor. The peripheral F_1 module $\alpha_3\beta_3\gamma\epsilon$ was incorporated into the membrane by forming the complex $\alpha_3\beta_3\gamma\epsilon c_{10}$ with the c_{10} ring. Finally, the F_0 module ab_2 bind with $\alpha_3\beta_3\gamma\epsilon c_{10}$ by the gluing of peripheral subunit δ in Figure 5(b). With binding rates all set to 10^5 M^{-1} s^{-1}, one pair of dead-end assembly intermediates $\alpha_3\beta_3\gamma\epsilon\delta c_{10}$ and δab_2 accumulated up to 18, undermining the assembly

efficiency of holo ATP synthase. We probe the modular assembly landscape of ATP synthase by changing the binding rates between certain intermediates or adding reverse dissociation reactions to see the impacts (Detailed reaction schemes in Table S4). For alternative assembly landscapes, beyond the uniform setting of 10^5 M^{-1} s^{-1}, 50 independent cell replicates were simulated for each case to capture statistical variation.

In Figure 5(c), slowing the binding rates between the c subunit oligomers, c_i, $(i = 2 \ldots 9)$, increases their accumulation, but cannot increase the formation of complete ATP synthase, since the c_{10} ring was cumulated in both cases. We tested three different strategies by changing the assembly rates or reactions to eliminate the non-functional structures, the pair of dead-end assembly intermediates $\alpha_3\beta_3\gamma\epsilon\delta c_{10}$ and δab_2, which the major challenge for high assembly yield as discussed by Murugan *et. al.*[75] Decreasing the binding rate between the $\alpha_3\beta_3\gamma\epsilon$ and the c_{10}-ring suppressed the accumulation of the dead-end complex $\alpha_3\beta_3\gamma\epsilon\delta c_{10}$, thus increasing the generated holocomplex to 69. Discriminating the association of the glue δ subunit with $\alpha_3\beta_3\gamma\epsilon c_{10}$ further increased the final generation of the complex to 70 (65% of the initial 108). Adding the dissociation reactions of two dead-end complexes while making the dissociation of the unstable $\alpha_3\beta_3\gamma\epsilon c_{10}$ intermediate faster 10^{-2} s^{-1} could also upgrade the generation of the final ATP synthase up to 70. As further evidence, the unassembled accumulation of the assembly intermediates also decreased in all three strategies. All three of these strategies could be used *in vivo* to increase efficiency in the modular assembly of ATP synthase.

Time-dependent cell behavior from the augumented WCM Syn3A

In the preceding sections, we discussed the various factors influencing the assembly of macromolecular holocomplexes. After including the assembly kinetics and pathways into the previously published WCM Syn3A, we now examine in greater detail the fundamental cellular behaviors over the cell cycle of $\sim$ 100 minutes.

We first consider DNA replication and doubling of cell volume and surface area. The

higher DnaA binding rate with ssDNA gives unrealistic fast replication initiation between 0.5 and 2.25 min with the mean of 1 min in Figure 6(a), which means a very short B period. However, the 4DWCM including the explicit diffusion of DnaA predicted a longer initiation time of mean time 5.5 min, where some cell replicates requiring 10 min or longer to form the DnaA filament and initiate DNA replication.[76] Changing back to the slower DnaA binding rate in the spatially homogeneous CME-ODE WCM, the expected initiation time recovered with the median of 5 min. This highlights the influence of diffusion on the cellular behaviors, and the necessity to adopt different parameterization strategies with and without considering diffusion.

There is a wide spread of times when each gene is copied. Starting with only one copy of the chromosome, second copies of genes near the terminus like *fakA*/0420 are available for transcription after 40 min in Figure S7(b). On average, the entire chromosome was duplicated around 49 minutes as shown in Figure 6(b), 20 min faster than the predicted time in the previous spatially homogeneous model in[6] where a slower DnaA binding rate was used. Apart from a faster initiation in this model, the main reason was the reduced halting of DNA replication from the shortage of deoxyribonucleotide monomers, as shown by the scaled replication rate in Figure 6(c). The DNA replication rate only dropped 10% in contrast to 25% drop in the previous model.[6] The elongation rates for transcription, and translation all show a slight decrease over parts of the cell cycle in Figure S7(d,e), but the majority cells are able to recover the monomer pools, and no cells were observed to run out of phosphoenol pyruvate (pep).

Cell volume doubled at a median time of 67 minutes in Figure 6(a), after which the partitioning of the chromosomes is assumed to occur. The cell cycle, defined as the time for surface area to double and the cells to divide, ranged from 93 to 112 with a median of 102 min in Figure S7(c), which is in good agreement with experimental measured 105 min.[2–4]

Once the simulation passes the initial transient, the active fractions of RNAP, ribosomes, and degradosomes stabilize at 65%, 73%, and 14%, respectively. The value for RNAP is high

compared to the values for naturally occurring bacteria that typically have a larger RNAP to gene ratio.[77] The active ratios maintained at steady-state due to the synchronized assembly of all three complexes along with the cell cycle that nearly double the initial complexes at the of the cycle in Figure S7(f).

The discreteness and stochasticity of protein synthesis is intrinsic at the single-cell level. A clear step-like trace of the synthesized protein FtsY/0429 is shown in Figure 6(d), where the stalled protein synthesis in the horizontal regions corresponded to no ribosomes translating this mRNA.

Upon transcription, the fate of the mRNAs is determined by the competition between its binding and translation by ribosomes into a protein, and its binding and degradation by degradosomes into NMPs. If one views the competition between the ribosome and the degradosome as a series of independent Bernoulli trials, where success means mRNA binding with the ribosome, and failure binding with the degradosome, then the distribution of the number of successes until the first failure occurs, which is the translations per mRNA transcript until mRNA degradation, follows a geometric distribution with the mean being the ratio of success over loss. The time-dependent ratio of mRNA binding with ribosome over binding over degradosome was calculated using $\frac{k_{bind}^{mRNA:Ribo} \times \# \, Free \, Ribosome}{k_{bind}^{mRNA:Deg} \times \# \, Free \, Degradosome}$. In our current implementations, the ratio between ribosome and degradosome binding rates was 6.3 ($\frac{k_{bind}^{mRNA:Ribo}}{k_{bind}^{mRNA:Deg}} = \frac{8.9 \times 10^4 \, \mathrm{M}^{-1}\mathrm{s}^{-1}}{1.4 \times 10^4 \, \mathrm{M}^{-1}\mathrm{s}^{-1}} = 6.3$). The number of available ribosomes over available degradosome was about 1.3 over the cell cycle, which further favor the mRNA to translation instead of degradation ($\frac{\# \, Free \, Ribosome}{\# \, Free \, Degradosome} = \frac{\#Total \;\; Ribosome \times (1 - \%Active \;\; Ribosome)}{\#Total \;\; Degradoeoms \times (1 - \%Active \;\; Degradosome)} \approx 1,3$). Thus, the mean of translation per mRNA as $\frac{k_{bind}^{mRNA:Ribo} \times \# \, Free \, Ribosome}{k_{bind}^{mRNA:Deg} \times \# \, Free \, Degradosome}$ was 8.2. From our simulation, the translation events per each unique mRNA transcript were calculated by dividing the number of translated proteins by the transcribed mRNAs. The distribution ranged from 4.8 to 11, with a prominent peak around 7.7 that was close to the calculated 8.2 in Figure S7(h).

An important metric of WCM Syn3A is whether the protein abundances are duplicated

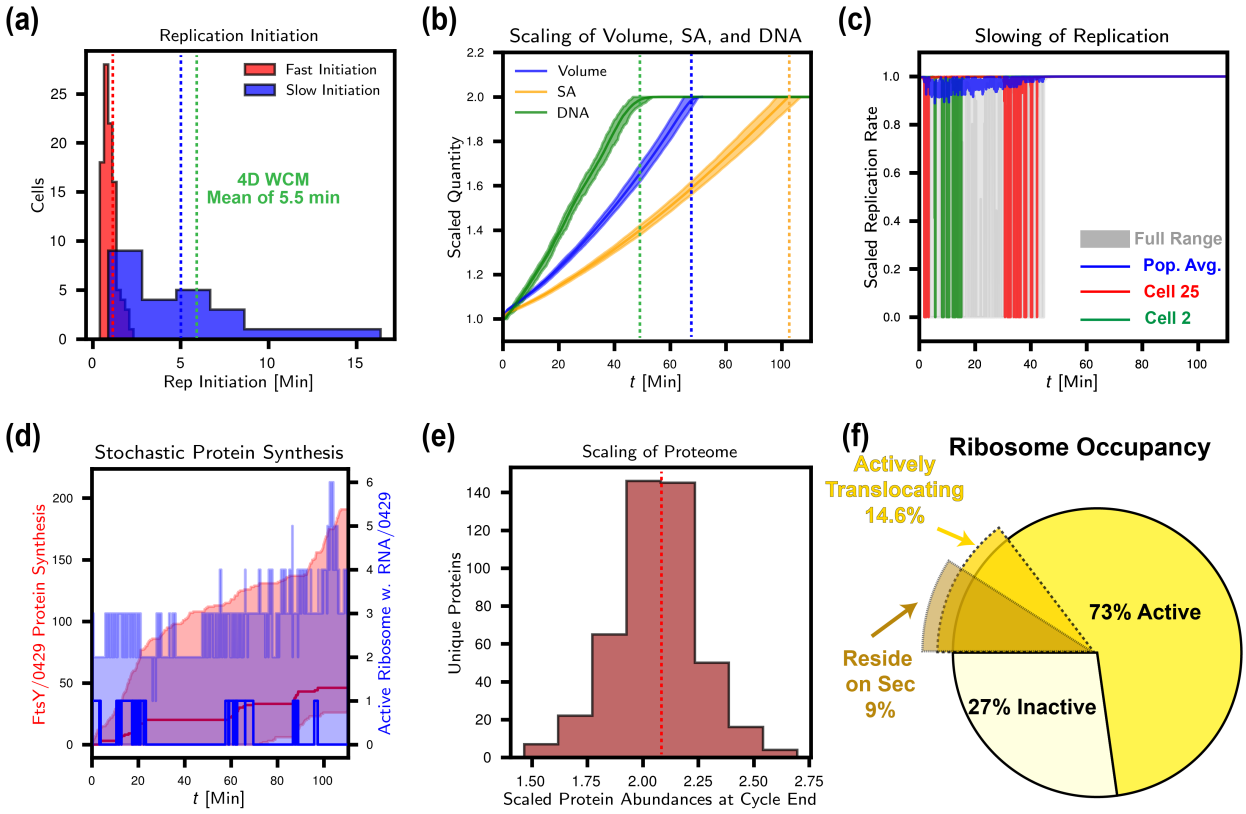

Figure 6: Time-dependent cell behavior from the augumented WCM Syn3A (a) Comparison of replication initiation time with fast and slow DnaA binding rate with ssDNA with median of 1 and 5 min, respectively. The median time from 4DWCM is shown by green line. (b) Scaled chromosome, volume and surface area over the entire cell cycle. (c) Slowing down of gene replication due to the dTTP shortage. In cell replicates 2 and 25 that running out of dTTP, the replication rate was zero at a temporal resolution of 1 second, and recovered with dTTP synthesis in nucleotide metabolism. The population averaged replication rate fell to 90% of the maximum (the blue line), and the gray shaded area shows the full range of scaled replication rate. (d) Stochastic gene expression of FtsY/0429. The left y-axis is the synthesized FtsY/0429, and the right is the active ribosome translating the mRNA of FtsY/0429. The solid lines represent one single cell replicate, the shaded areas the full range. (e) Distribution of population averaged scaled protein abundance at the end of cell cycle with the median of 2.07. (f) Ribosome occupancy at steady-state. 73% out of total are actively translating mRNAs, 14.6% out of total are active in translocation of transmembrane proteins and lipoproteins, and 9% out of total are residing on Sec translocon.

at the end of the cell cycle as division is completed. The averaged scaled protein abundances range from 1.46 to 2.71, with only 32 of the 452 proteins having a value less than 1.8 in Figure 6(e). Two factors contributing to the distribution of the scaled abundance are the length of the protein and the initial proteomics counts. Shorter proteins with the lower initial counts will favor a higher scale abundance. Proteins longer than 1000 AAs or with initial counts greater than 800 almost failed to double over the course of a cell cycle. Polysomes, not included in this WCM, would serve as a mechanism to increase the expression levels of long proteins.[6] Proteins with low or zero initial counts in the proteomics data were assigned an initial count of 10, and these proteins are the majority of proteins with scaled abundance was greater than 2.4. While it is not clear whether multiple rounds of the cell cycle would narrow the distribution, improvement in the proteomics annotations of protein subunits in the membrane would improve the analysis. The exact values of scaled protein abundances are in File S2.

In the current translation and translocation network, the failure of cotranslational translocation of membrane proteins was considered to lead to the degradation of membrane proteins by FtsH, the membrane embedded protease. The predicted failure rate of targeting transmembrane proteins ranged from 4% to 8% with median 6.9%, and for lipoproteins, the rates were lower with a median of 3.5%, consistent with an experimental observation.[78] The loss due to degradation slightly undermine the doubling of membrane proteins. The degradation of transmembrane proteins by FtsH to recycle free amino acids was minor compared to amino acid import via passive permeases and active ABC transporter, Opp in Figure S8(a,b). However, the analysis of amino acids' economy and doubling of proteome could be improved by the degradation of cytoplasmic proteins by another protease, encoded by *Lon*/394.[79]

From the translocation network, we could also further differentiate the occupancy states of ribosome in Figure 6(f). The active ratio of ribosome at steady-state was 73% out of total on the population average as stated before. The active ribosomes are directed to the plasma membrane by the targeting factors SRP/SR and SecA for transmembrane proteins

and secretory proteins, respectively. The ratio of ribosomes in SRP/SR/Sec and SecA/Sec translocation pathways over the active ribosomes was 20% ($\frac{14.6\%}{73\%}$) at steady state. This ratio of 20% was closely related to the summed mRNA counts of the transmembrane protein and secretory protein encoding mRNAs over the total summed mRNA counts that could be roughly estimated by the ratio of genes encoding transmembrane proteins and secretory proteins, which is $\frac{84+15}{455} = 21\%$. As a subset of ribosomes in two translocation pathways, the predicted ratio of the ribosome that resides in the Sec translocon was lower at 9% out of the total ribosomes. Based on cryo-ET images,[10] we were also able to estimate this ratio by counting the ribosomes that were located 11 nm from the cell membrane. 11 nm, as half the ribosome size of 21 nm[80] was selected due to the very close contact between the RNC and the Sec translocon.[81] Two cryo-ETs gave ratios $13\% = \frac{67}{503}$ and $9\% = \frac{72}{820}$, which supported our simulation. Of the involved translocation entities, the Sec translocon was the most active with a ratio of 78% due to the small number of Sec translocons compared to the ribosomes for transmembrane proteins and secretory proteins.

Analysis of time-dependent cell metabolomics

The machine learning analysis of the time-dependent metabolite concentrations identified three distinct cell lineages 1, 2, and 3 that consist of 10, 24, and 63 cells, respectively. In the following, we refer to the cell lineage as a cell population. Metabolic profile divergence occurs at approximately 20 min for the populations 1-2, 8 min for 1-3, and 21 min for 2-3, the early stage of the cell cycle. Key metabolites were determined using two-sample t-tests, and the magnitudes of these differences using standard effect sizes (Cohen's d statistic). The results are presented in Figure 7.

Cell population 1 is small (10% of the entire cell population) compared to populations 2 and 3. Accumulation of ATP and phosphoribosyl pyrophosphate (prpp), that converts nucleic base to monophosphate nucleoside) made population 1 separate from 2 and 3, meanwhile increasing the import of ions calcium (ca^{2+}), potassium (k^{+}), and spermine ($sprm_{4+}$)

through their ATP activated transporters. The mean concentration of ATP at the end of the cell cycle in cell population 1 was nearly 20 mM, and less than 10 mM for populations 2 and 3. The correlation between ATP and activated transport is also supported by the higher fluxes for cell population 1 for the uptake of amino acids by ABC transporter OPP identified in Figure S9(a,b).

The concentration of the magnesium ions that are imported has been modified to account for its near irreversible binding to negatively charged nucleic acids giving a relatively low concentration of free ions in the cell (not shown). The correction was made by subtracting off the number of ions typically observed in the structures of ribosomes and (d)NTPs. The high resolution PDB 4V5D structure of the bacterial ribosome[82] contains 1346 Mg^{2+} and each (d)NTP molecule binds to 1 Mg^{2+} cation. The concentrations of the other ions are similar to reported cellular concentrations.

The differences between populations 2 and 3 were more subtle and require examination of the metabolic maps in Figure S1, and variation of time-dependent metabolites concentrations (Figure 7(c,f)) and reaction fluxes (Figure S9(c)) between the two cell lineages. In population 3, accumulation of the upstream glycolytic metabolites D-Glucose 6-phosphate (g6p) and D-Fructose 6-phosphate (f6p) corresponds to lower productions of ATP and higher fluxes through reactions in the lipid metabolism that branches off from g6p, specifically giving rise to higher concentrations of cardiolipins (clpn). The intermediate metabolites in the pentose pathway, D-Ribulose 5-phosphate (ru5p) and D-Xylulose 5-phosphate (xu5p) that also branches off from g6p are more accumulated in population 3.

Conclusions

In the context of the WCM, we showed that the efficiency of complex assembly can be significantly hindered by the reduction in the assembly rate from 10^5 to 10^3 $M^{-1}s^{-1}$. We rationalize this using a simplified dimerization model that showed a reduction of unassembled

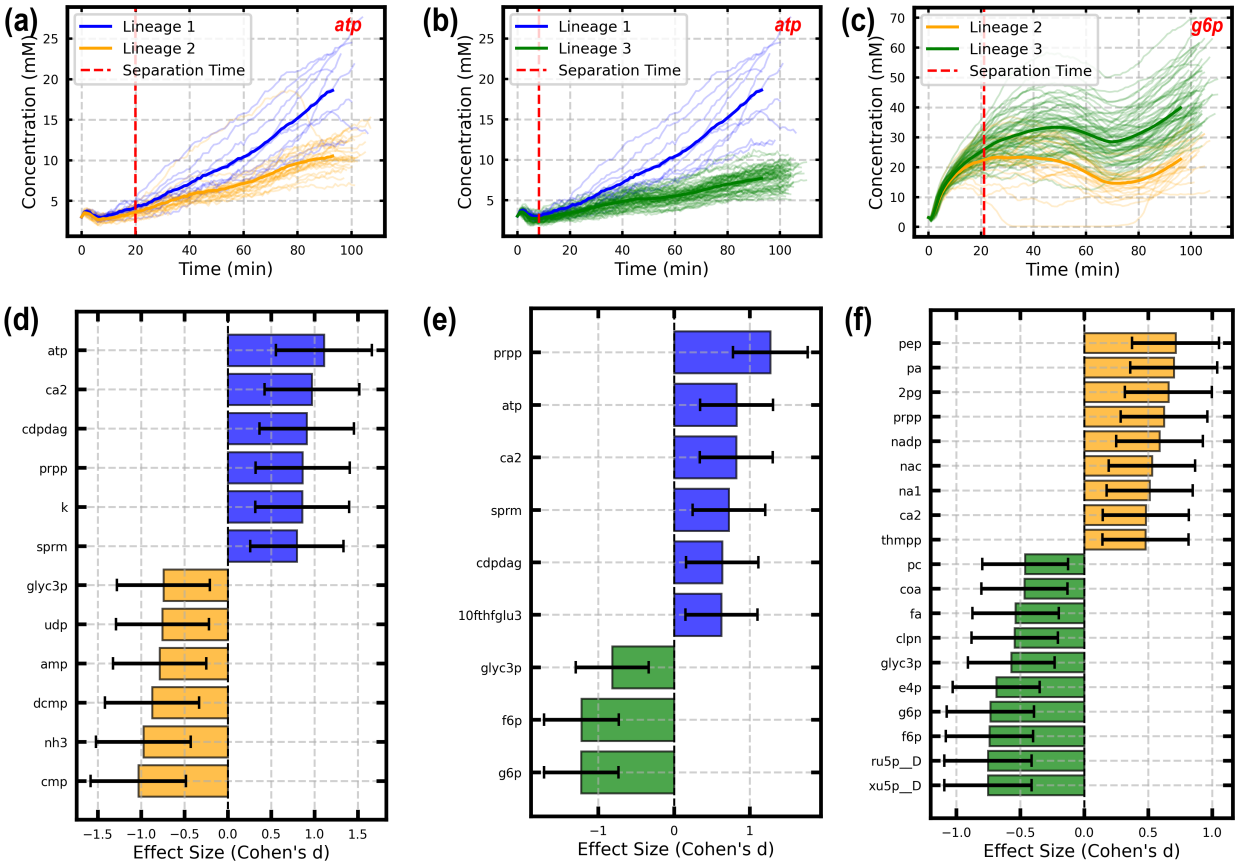

Figure 7: Differential metabolites and their abundances for each pair of populations. (a) Time-dependent ATP concentration in cell population 1 and 2. (b) Time-dependent ATP concentration in cell population 1 and 3. (c) Time-dependent g6p concentration in cell population 2 and 3. (d) Identified differential metabolites for cell population 1 (blue) and 2 (orange). (e) Identified differential metabolites for cell population 1 (blue) and 3 (green). (f) Identified differential metabolites for cell population 2(orange) and 3 (green). The colored boxes as the effect size indicate which population (blue is 1, orange is 2, and green is 3) has the larger abundance of the metabolite. The black bars show the 95% confidence interval of the effect size, and the absence of zero indicates the difference are statistically significant.

complexes as assembly rate is increased. This highlights the temporal coupling of gene expression and complex assembly at the whole-cell scale that was not previously reported.

The non-stoichiometric synthesis of protein subunits at the single-cell level was highlighted using ATP synthase, which comprises eight subunits with distinct stoichiometries. This observation underscores the need to incorporate co-expression from polycistronic mRNA isoforms into the transcription model.

In addition to capturing complex formation, our model successfully predicted the collective behavior of cellular dynamics. The simulated cell cycle durations—defined as the time required to double the cell surface area—ranged from 96 to 110 minutes, in agreement with experimental measurements.[2–4] The total proteome approximately doubled by the end of the cell cycle, with reasonable deviations discussed elsewhere. We quantified mRNA translation efficiency based on mRNA binding rates and the availability of ribosomes and degradosomes, the latter of which were influenced by macromolecular complex assembly. The integrated whole-cell translation and translocation networks enabled us to estimate that approximately 9% of ribosomes were associated with the Sec translocon, consistent with experimental observations of a number of ribosomes near the cell membrane in Syn3A.[7]

Furthermore, a novel deep learning-based trajectory inference analysis of time-dependent metabolic profiles revealed the emergence of three distinct cell populations, with bifurcation occurring early in the cell cycle. Key glycolytic metabolites were identified as potential drivers of this divergence.

Limitation and Outlook

The simulations discussed were performed under the spatially homogeneous assumption (CME and ODE), which ignores the spatial heterogeneity of bacterial cells. Therefore, processes such as the diffusion of DNA, RNA, and proteins are not considered and respective impacts on cellular dynamics are absent from our model. The differences resulting from the spatially homogeneous assumption are evident when the WCM model presented here

is compared to a recently reported spatial WCM model (4DWCM).[76] For example, DNA replication initiation within the spatially homogeneous simulations happens roughly twice as fast as in the 4DWCM. The difference in cellular behaviors results from diffusion that affects the binding of the protein that initiates DNA replication, DnaA. We predict that the dynamics of other processes such as complex formation or protein translocation would be impacted if spatial heterogeneity was considered in our model. Although the spatially homogeneous assumption is limited, it has a significant advantage in its significantly reduced computational demands, providing the ability to test a wide range of parameters in tens to hundreds of replicate cells, especially in comparison to the computational demands of spatial models.[76]

Our model provides a unique ability to capture the dynamics of many cellular components simultaneously, predicting more quantities than can be measured in any single experiment, however our representation of bacterial life is incomplete. In our simulations, there are missing bacterial processes that are understood to be important in the stoichiometric expression of proteins.[74] Most notable is in the gene expression model, polycistronic mRNAs were not considered and genes were expressed independently. We found that the heterogeneity of the subunit synthesis of the same complex (e.g. ATP synthase) at the single-cell level heavily undermined the efficiency of complex formation from the supply-side. We predict by facilitating the co-expression of subunits with polycistronic mRNAs in operons, the complex assembly efficiency will be improved, as demonstrated in a WCM of *E. coli*.[83] Currently, efforts are underway to characterize polycistronic mRNA isoforms using long-read RNA sequencing data. With this data, the gene expression model could be refined to recapitulate the transcriptome (and thus the proteome) as has been experimentally observed in Syn3A.

Acknowledgement

E.F and Z.LS are partially supported by NSF MCB-2221237 and the NSF Science and Technology Center for Quantitative Cell Biology (NSF DBI-2243257), T.B and B.G are partially supported by NSF MCB-2221237. S.W., B.Y., and R.W are partially supported by NSF DMS-2515171 and the NSF Science and Technology Center for Quantitative Cell Biology (NSF DBI-2243257).

Z.R.T.: Research reported in this publication was supported by the Cancer Center at Illinois - Beckman Institute Postdoctoral Fellows Program sponsored by the Cancer Center at Illinois and the Beckman Institute for Advanced Science and Technology, University of Illinois Urbana-Champaign. The content is solely the responsibility of the authors and does not necessarily represent the official views of the program sponsors.

Supporting Information Available

The simulation code is available on GitHub at `https://github.com/Luthey-Schulten-Lab/Minimal_Cell_ComplexFormation`.

The Supporting Information is available free of charge.

- File S1 Supporting Information. Metabolic networks with annotated protein complexes, reactions of gene expression model, compositions and assembly pathways of complexes, translocation network, derivation of unassembled fraction, SI Table S1-S10, SI Figure S1-S9

- File S2 Proteome, initial mRNA counts, and initial metabolites concentrations. Tab 1 Comparative Proteomics: Comparative proteomics of Syn3A to other with the revised annotations and localizations of Syn3A's proteome; annotations of certain proteins updated based on[5] noted by slash separation. Tab 2 Protein Topologies: Prediction of signal peptide and transmembrane regions from SignalP and DeepTMHMM. Tab

3 Scaled Proteome: Partitioning of the proteomics counts for complex subunits; the scaled abundances of all proteins at the end of cell cycle. Tab 4 mRNA Count: Initial average count of mRNAs. Tab 5 Intracellular Metabolites: Initial concentrations of intracellular metabolites, and time-averaged concentrations of intracellular metabolites. Tab 6 Experimental Medium: Experimental Defined Medium. Tab 7 Simulation Medium: Simulation Defined Medium.

- File S3 kinetic parameters. Tab 1 Central: Kinetic parameter for central metabolism. Tab 2 Nucleotide: Kinetic parameter for nucleotide metabolism. Tab 3 Lipid: Kinetic parameter for lipid metabolism. Tab 4 Cofactor: Kinetic parameter for cofactor metabolism. Tab 5 Transport: Kinetic parameter for metabolic transport reactions. Tab 6 Non-Random-Binding Reactions: Kinetic parameter for non-random binding reactions. Tab 7 tRNA charging: Kinetic parameter for tRNA charging. Tab 8 Gene Expression: Kinetic parameters for gene expression. Tab 9 SSU Assembly: Assembly reactions and rates for ribosome SSU. Tab 10 LSU Assembly: Assembly reactions and rates of ribosome LSU.

- File S4 ML on metabolomics: Machine learning analysis on metabolomics with the traces of differential metabolites and reactions for all 3 lineage pairs

- File S5 Trajectories of all time-dependent metabolite concentrations and metabolic fluxes. Solid lines represent the population averages. Shaded regions represent the ranges observed for the entire population of simulated cell.

References

(1) Hutchison, C. A. et al. Design and synthesis of a minimal bacterial genome. *Science* **2016**, *351*, aad6253, Publisher: American Association for the Advancement of Science.

(2) Breuer, M. et al. Essential metabolism for a minimal cell. *eLife* **2019**, *8*, e36842, Publisher: eLife Sciences Publications, Ltd.

(3) Pelletier, J. F.; Sun, L.; Wise, K. S.; Assad-Garcia, N.; Karas, B. J.; Deerinck, T. J.; Ellisman, M. H.; Mershin, A.; Gershenfeld, N.; Chuang, R.-Y.; Glass, J. I.; Strychalski, E. A. Genetic requirements for cell division in a genomically minimal cell. *Cell* **2021**, *184*, 2430–2440.e16.

(4) Sandberg, T. E.; Wise, K. S.; Dalldorf, C.; Szubin, R.; Feist, A. M.; Glass, J. I.; Palsson, B. O. Adaptive evolution of a minimal organism with a synthetic genome. *iScience* **2023**, *26*, 107500.

(5) Bianchi, D. M.; Pelletier, J. F.; Hutchison, C. A.; Glass, J. I.; Luthey-Schulten, Z. Toward the Complete Functional Characterization of a Minimal Bacterial Proteome. *The Journal of Physical Chemistry B* **2022**, *126*, 6820–6834.

(6) Thornburg, Z. R.; Bianchi, D. M.; Brier, T. A.; Gilbert, B. R.; Earnest, T. M.; Melo, M. C.; Safronova, N.; Sáenz, J. P.; Cook, A. T.; Wise, K. S.; Hutchison, C. A.; Smith, H. O.; Glass, J. I.; Luthey-Schulten, Z. Fundamental behaviors emerge from simulations of a living minimal cell. *Cell* **2022**, *185*, 345–360.e28, Publisher: Elsevier.

(7) Gilbert, B. R.; Thornburg, Z. R.; Lam, V.; Rashid, F.-Z. M.; Glass, J. I.; Villa, E.; Dame, R. T.; Luthey-Schulten, Z. Generating Chromosome Geometries in a Minimal Cell From Cryo-Electron Tomograms and Chromosome Conformation Capture Maps. *Frontiers in Molecular Biosciences* **2021**, *8*, 644133.

(8) Thornburg, Z. R.; Melo, M. C. R.; Bianchi, D.; Brier, T. A.; Crotty, C.; Breuer, M.; Smith, H. O.; Hutchison, C. A.; Glass, J. I.; Luthey-Schulten, Z. Kinetic Modeling of the Genetic Information Processes in a Minimal Cell. *Frontiers in Molecular Biosciences* **2019**, *6*, 130.

(9) Bianchi, D. M.; Peterson, J. R.; Earnest, T. M.; Hallock, M. J.; Luthey-Schulten, Z. Hybrid CME–ODE method for efficient simulation of the galactose switch in yeast. *IET Systems Biology* **2018**, *12*, 170–176, _eprint: https://onlinelibrary.wiley.com/doi/pdf/10.1049/iet-syb.2017.0070.

(10) Gilbert, B. R.; Thornburg, Z. R.; Brier, T. A.; Stevens, J. A.; Grunewald, F.; Stone, J. E.; Marrink, S. J.; Luthey-Schulten, Z. Dynamics of chromosome organization in a minimal bacterial cell. *Biophysical Journal* **2024**, *123*, 327a.

(11) Du Plessis, D. J.; Nouwen, N.; Driessen, A. J. The Sec translocase. *Biochimica et Biophysica Acta (BBA) - Biomembranes* **2011**, *1808*, 851–865.

(12) Murakami, K. Structural Biology of Bacterial RNA Polymerase. *Biomolecules* **2015**, *5*, 848–864.

(13) Davis, J. H.; Tan, Y. Z.; Carragher, B.; Potter, C. S.; Lyumkis, D.; Williamson, J. R. Modular Assembly of the Bacterial Large Ribosomal Subunit. *Cell* **2016**, *167*, 1610–1622.e15.

(14) Deckers-Hebestreit, G. Assembly of the *Escherichia coli* FoF1 ATP synthase involves distinct subcomplex formation. *Biochemical Society Transactions* **2013**, *41*, 1288–1293.

(15) Chen, S. S.; Sperling, E.; Silverman, J. M.; Davis, J. H.; Williamson, J. R. Measuring the dynamics of E. coli ribosome biogenesis using pulse-labeling and quantitative mass spectrometry. *Molecular BioSystems* **2012**, *8*, 3325.

(16) Matsubayashi, H.; Kuruma, Y.; Ueda, T. In Vitro Synthesis of the *E. coli* Sec Translocon from DNA. *Angewandte Chemie International Edition* **2014**, *53*, 7535–7538.

(17) Dong, X.; Doerfel, L. K.; Sheng, K.; Rabuck-Gibbons, J. N.; Popova, A.; Lyumkis, D.; Williamson, J. Near-physiological *in vitro* assembly of 50S ribosomes involves parallel pathways. *Nucleic Acids Research* **2023**, *51*, 2862–2876.

(18) Brockmann, B.; Koop Genannt Hoppmann, K. D.; Strahl, H.; Deckers-Hebestreit, G. Time-Delayed In Vivo Assembly of Subunit a into Preformed Escherichia coli FoF1 ATP Synthase. *Journal of Bacteriology* **2013**, *195*, 4074–4084.

(19) Berg, O. G.; von Hippel, P. H. Diffusion-Controlled Macromolecular Interactions. *Annual Review of Biophysics* **1985**, *14*, 131–158, Publisher: Annual Reviews Type: Journal Article.

(20) Yogurtcu, O. N.; Johnson, M. E. Cytosolic proteins can exploit membrane localization to trigger functional assembly. *PLOS Computational Biology* **2018**, *14*, e1006031, Publisher: Public Library of Science.

(21) Held, W. A.; Ballou, B.; Mizushima, S.; Nomura, M. Assembly Mapping of 30 S Ribosomal Proteins from Escherichia coli. *Journal of Biological Chemistry* **1974**, *249*, 3103–3111.

(22) Herold, M.; Nierhaus, K. H. Incorporation of six additional proteins to complete the assembly map of the 50 S subunit from Escherichia coli ribosomes. *Journal of Biological Chemistry* **1987**, *262*, 8826–8833.

(23) Sheng, K.; Li, N.; Rabuck-Gibbons, J. N.; Dong, X.; Lyumkis, D.; Williamson, J. R. Assembly landscape for the bacterial large ribosomal subunit. *Nature Communications* **2023**, *14*, 5220.

(24) Earnest, T.; Lai, J.; Chen, K.; Hallock, M.; Williamson, J.; Luthey-Schulten, Z. Toward a Whole-Cell Model of Ribosome Biogenesis: Kinetic Modeling of SSU Assembly. *Biophysical Journal* **2015**, *109*, 1117–1135.

(25) Earnest, T. M.; Cole, J. A.; Peterson, J. R.; Hallock, M. J.; Kuhlman, T. E.; Luthey-Schulten, Z. Ribosome biogenesis in replicating cells: Integration of experiment and theory. *Biopolymers* **2016**, *105*, 735–751, _eprint: https://onlinelibrary.wiley.com/doi/pdf/10.1002/bip.22892.

(26) Earnest, T. M.; Watanabe, R.; Stone, J. E.; Mahamid, J.; Baumeister, W.; Villa, E.; Luthey-Schulten, Z. Challenges of Integrating Stochastic Dynamics and Cryo-Electron Tomograms in Whole-Cell Simulations. *The Journal of Physical Chemistry B* **2017**, *121*, 3871–3881, Publisher: American Chemical Society.

(27) Thomas, C.; Tampé, R. Structural and Mechanistic Principles of ABC Transporters. *Annual Review of Biochemistry* **2020**, *89*, 605–636.

(28) Webb, A. J.; Hosie, A. H. F. A Member of the Second Carbohydrate Uptake Subfamily of ATP-Binding Cassette Transporters Is Responsible for Ribonucleoside Uptake in *Streptococcus mutans*. *Journal of Bacteriology* **2006**, *188*, 8005–8012.

(29) Hegde, R. S.; Keenan, R. J. The mechanisms of integral membrane protein biogenesis. *Nature Reviews Molecular Cell Biology* **2022**, *23*, 107–124.

(30) Hegde, R. S.; Keenan, R. J. A unifying model for membrane protein biogenesis. *Nature Structural & Molecular Biology* **2024**, *31*, 1009–1017.

(31) Wen, J.-H.; He, X.-H.; Feng, Z.-S.; Li, D.-Y.; Tang, J.-X.; Liu, H.-F. Cellular Protein Aggregates: Formation, Biological Effects, and Ways of Elimination. *International Journal of Molecular Sciences* **2023**, *24*, 8593.

(32) Schlosshauer, M.; Baker, D. Realistic protein–protein association rates from a simple diffusional model neglecting long-range interactions, free energy barriers, and landscape ruggedness. *Protein Science* **2004**, *13*, 1660–1669.

(33) Schreiber, G.; Haran, G.; Zhou, H.-X. Fundamental Aspects of Protein-Protein Association Kinetics. *Chemical Reviews* **2009**, *109*, 839–860.

(34) Karr, J.; Sanghvi, J.; Macklin, D.; Gutschow, M.; Jacobs, J.; Bolival, B.; Assad-Garcia, N.; Glass, J.; Covert, M. A Whole-Cell Computational Model Predicts Phenotype from Genotype. *Cell* **2012**, *150*, 389–401.

(35) Macklin, D. N. et al. Simultaneous cross-evaluation of heterogeneous *E. coli* datasets via mechanistic simulation. *Science* **2020**, *369*, eaav3751.

(36) Rühle, T.; Leister, D. Assembly of F1F0-ATP synthases. *Biochimica et Biophysica Acta (BBA) - Bioenergetics* **2015**, *1847*, 849–860.

(37) Hallock, M. J.; Stone, J. E.; Roberts, E.; Fry, C.; Luthey-Schulten, Z. Simulation of reaction diffusion processes over biologically relevant size and time scales using multi-GPU workstations. *Parallel Computing* **2014**, *40*, 86–99.

(38) Abramson, J. et al. Accurate structure prediction of biomolecular interactions with AlphaFold 3. *Nature* **2024**, *630*, 493–500.

(39) Hinton, G. E.; Salakhutdinov, R. R. Reducing the dimensionality of data with neural networks. *Science* **2006**, *313*, 504–507.

(40) Street, K.; Risso, D.; Fletcher, R. B.; Das, D.; Ngai, J.; Yosef, N.; Purdom, E.; Dudoit, S. Slingshot: cell lineage and pseudotime inference for single-cell transcriptomics. *BMC Genomics* **2018**, *19*, 477.

(41) Roberts, E.; Stone, J. E.; Luthey-Schulten, Z. Lattice microbes: High-performance stochastic simulation method for the reaction-diffusion master equation. *Journal of Computational Chemistry* **2013**, *34*, 245–255, _eprint: https://onlinelibrary.wiley.com/doi/pdf/10.1002/jcc.23130.

(42) Peterson, J. R.; Hallock, M. J.; Cole, J. A.; Luthey-Schulten, Z. A Problem Solving Environment for Stochastic Biological Simulations. **2013**, Publisher: Unpublished.

(43) Cheng, H.-M.; Gröger, P.; Hartmann, A.; Schlierf, M. Bacterial initiators form dynamic filaments on single-stranded DNA monomer by monomer. *Nucleic Acids Research* **2015**, *43*, 396–405.

(44) Mika, J. T.; Schavemaker, P. E.; Krasnikov, V.; Poolman, B. Impact of osmotic stress on protein diffusion in *L* *actococcus lactis*. *Molecular Microbiology* **2014**, *94*, 857–870.

(45) Grasberger, B.; Minton, A. P.; DeLisi, C.; Metzger, H. Interaction between proteins localized in membranes. *Proceedings of the National Academy of Sciences* **1986**, *83*, 6258–6262.

(46) Tsukazaki, T.; Mori, H.; Echizen, Y.; Ishitani, R.; Fukai, S.; Tanaka, T.; Perederina, A.; Vassylyev, D. G.; Kohno, T.; Maturana, A. D.; Ito, K.; Nureki, O. Structure and function of a membrane component SecDF that enhances protein export. *Nature* **2011**, *474*, 235–238.

(47) Chatzi, K. E.; Sardis, M. F.; Economou, A.; Karamanou, S. SecA-mediated targeting and translocation of secretory proteins. *Biochimica et Biophysica Acta (BBA) - Molecular Cell Research* **2014**, *1843*, 1466–1474.

(48) Zhu, Z.; Wang, S.; Shan, S.-o. Ribosome profiling reveals multiple roles of SecA in cotranslational protein export. *Nature Communications* **2022**, *13*, 3393.

(49) Schibich, D.; Gloge, F.; Pöhner, I.; Björkholm, P.; Wade, R. C.; Von Heijne, G.; Bukau, B.; Kramer, G. Global profiling of SRP interaction with nascent polypeptides. *Nature* **2016**, *536*, 219–223.

(50) Zhang, X.; Schaffitzel, C.; Ban, N.; Shan, S.-o. Multiple conformational switches in a GTPase complex control co-translational protein targeting. *Proceedings of the National Academy of Sciences* **2009**, *106*, 1754–1759.

(51) Akopian, D.; Dalal, K.; Shen, K.; Duong, F.; Shan, S.-o. SecYEG activates GTPases to drive the completion of cotranslational protein targeting. *Journal of Cell Biology* **2013**, *200*, 397–405.

(52) Serdiuk, T.; Steudle, A.; Mari, S. A.; Manioglu, S.; Kaback, H. R.; Kuhn, A.; Müller, D. J. Insertion and folding pathways of single membrane proteins guided by translocases and insertases. *Science Advances* **2019**, *5*, eaau6824.

(53) Nouwen, N.; Driessen, A. J. M. SecDFyajC forms a heterotetrameric complex with YidC. *Molecular Microbiology* **2002**, *44*, 1397–1405.

(54) Elvekrog, M. M.; Walter, P. Dynamics of co-translational protein targeting. *Current Opinion in Chemical Biology* **2015**, *29*, 79–86.

(55) Burgos, R.; Weber, M.; Martinez, S.; Lluch-Senar, M.; Serrano, L. Protein quality control and regulated proteolysis in the genome-reduced organism *Mycoplasma pneumoniae*. *Molecular Systems Biology* **2020**, *16*, e9530.

(56) Akiyama, Y.; Kihara, A.; Tokuda, H.; Ito, K. FtsH (HflB) Is an ATP-dependent Protease Selectively Acting on SecY and Some Other Membrane Proteins. *Journal of Biological Chemistry* **1996**, *271*, 31196–31201, Publisher: Elsevier.

(57) Yang, Y.; Gunasekara, M.; Muhammednazaar, S.; Li, Z.; Hong, H. Proteolysis mediated by the membrane-integrated ATP-dependent protease FtsH has a unique nonlinear dependence on ATP hydrolysis rates. *Protein Science* **2019**, *28*, 1262–1275.

(58) Kaushik, S.; He, H.; Dalbey, R. E. Bacterial Signal Peptides- Navigating the Journey of Proteins. *Frontiers in Physiology* **2022**, *13*, 933153.

(59) Beck, K. Discrimination between SRP- and SecA/SecB-dependent substrates involves selective recognition of nascent chains by SRP and trigger factor. *The EMBO Journal* **2000**, *19*, 134–143.

(60) Tsukazaki, T. Structure-based working model of SecDF, a proton-driven bacterial protein translocation factor. *FEMS Microbiology Letters* **2018**, *365*.

(61) Nguyen, M.-T.; Matsuo, M.; Niemann, S.; Herrmann, M.; Götz, F. Lipoproteins in Gram-Positive Bacteria: Abundance, Function, Fitness. *Frontiers in Microbiology* **2020**, *11*, 582582.

(62) Legood, S.; Boneca, I. G.; Buddelmeijer, N. Mode of action of lipoprotein modification enzymes—Novel antibacterial targets. *Molecular Microbiology* **2021**, *115*, 356–365.

(63) Teufel, F.; Almagro Armenteros, J. J.; Johansen, A. R.; Gíslason, M. H.; Pihl, S. I.; Tsirigos, K. D.; Winther, O.; Brunak, S.; Von Heijne, G.; Nielsen, H. SignalP 6.0 predicts all five types of signal peptides using protein language models. *Nature Biotechnology* **2022**, *40*, 1023–1025.

(64) Hallgren, J.; Tsirigos, K. D.; Pedersen, M. D.; Almagro Armenteros, J. J.; Marcatili, P.; Nielsen, H.; Krogh, A.; Winther, O. DeepTMHMM predicts alpha and beta transmembrane proteins using deep neural networks. 2022; `http://biorxiv.org/lookup/doi/10.1101/2022.04.08.487609`.

(65) Bengio, Y.; LeCun, Y. Scaling learning algorithms towards AI. *Large-scale Kernel Machines* **2007**, *34*, 1–41.

(66) Ranzato, M.; Poultney, C.; Chopra, S.; Cun, Y. Efficient learning of sparse representations with an energy-based model. *Advances in Neural Information Processing Systems* **2006**, *19*.

(67) Eraslan, G.; Simon, L. M.; Mircea, M.; Mueller, N. S.; Theis, F. J. Single-cell RNA-seq denoising using a deep count autoencoder. *Nature Communications* **2019**, *10*, 390.

(68) Rong, Z.; Tan, Q.; Cao, L.; Zhang, L.; Deng, K.; Huang, Y.; Zhu, Z.-J.; Li, Z.; Li, K. NormAE: deep adversarial learning model to remove batch effects in liquid chromatography mass spectrometry-based metabolomics data. *Analytical Chemistry* **2020**, *92*, 5082–5090.

(69) Cogswell, M.; Ahmed, F.; Girshick, R.; Zitnick, L.; Batra, D. Reducing overfitting in deep networks by decorrelating representations. *arXiv preprint arXiv:1511.06068* **2015**,

(70) Bardes, A.; Ponce, J.; LeCun, Y. Variance-invariance-covariance regularization for self-supervised learning. *ICLR, Vicreg* **2022**, *1*.

(71) Street, K.; Risso, D.; Fletcher, R. B.; Das, D.; Ngai, J.; Yosef, N.; Purdom, E.; Dudoit, S. Slingshot: cell lineage and pseudotime inference for single-cell transcriptomics. *BMC Genomics* **2018**, *19*, 477.

(72) Benjamini, Y.; Hochberg, Y. Controlling the false discovery rate: a practical and powerful approach to multiple testing. *Journal of the Royal Statistical Society: Series B* **1995**, *57*, 289–300.

(73) Guo, H.; Suzuki, T.; Rubinstein, J. L. Structure of a bacterial ATP synthase. *eLife* **2019**, *8*, e43128.

(74) Taggart, J. C.; Lalanne, J.-B.; Li, G.-W. Quantitative Control for Stoichiometric Protein Synthesis. *Annual Review of Microbiology* **2021**, *75*, 243–267.

(75) Murugan, A.; Zou, J.; Brenner, M. P. Undesired usage and the robust self-assembly of heterogeneous structures. *Nature Communications* **2015**, *6*, 6203.

(76) Thornburg, Z. R. et al. Bringing the Genetically Minimal Cell to Life on a Computer in 4D. **2025**, Publisher: Cold Spring Harbor Laboratory.

(77) Bremer, H.; Dennis, P. P. Modulation of Chemical Composition and Other Parameters of the Cell at Different Exponential Growth Rates. *EcoSal Plus* **2008**, *3*, 10.1128/ecosal.5.2.3, Publisher: American Society for Microbiology.

(78) Hessa, T.; Sharma, A.; Mariappan, M.; Eshleman, H. D.; Gutierrez, E.; Hegde, R. S. Protein targeting and degradation are coupled for elimination of mislocalized proteins. *Nature* **2011**, *475*, 394–397.

(79) Gur, E.; Sauer, R. T. Evolution of the ssrA degradation tag in *Mycoplasma* : Specificity switch to a different protease. *Proceedings of the National Academy of Sciences* **2008**, *105*, 16113–16118.

(80) Schuwirth, B. S.; Borovinskaya, M. A.; Hau, C. W.; Zhang, W.; Vila-Sanjurjo, A.; Holton, J. M.; Cate, J. H. D. Structures of the Bacterial Ribosome at 3.5 Å Resolution. *Science* **2005**, *310*, 827–834.

(81) Lewis, A. J.; Zhong, F.; Keenan, R. J.; Hegde, R. S. Structural analysis of the dynamic ribosome-translocon complex. *eLife* **2024**, *13*, RP95814.

(82) Voorhees, R. M.; Weixlbaumer, A.; Loakes, D.; Kelley, A. C.; Ramakrishnan, V. Insights into substrate stabilization from snapshots of the peptidyl transferase center of the intact 70S ribosome. *Nature Structural & Molecular Biology* **2009**, *16*, 528–533.

(83) Sun, G.; DeFelice, M. M.; Gillies, T. E.; Ahn-Horst, T. A.; Andrews, C. J.; Krummenacker, M.; Karp, P. D.; Morrison, J. H.; Covert, M. W. Cross-evaluation of E. coli's operon structures via a whole-cell model suggests alternative cellular benefits for low- versus high-expressing operons. *Cell Systems* **2024**, *15*, 227–245.e7.

TOC Graphic

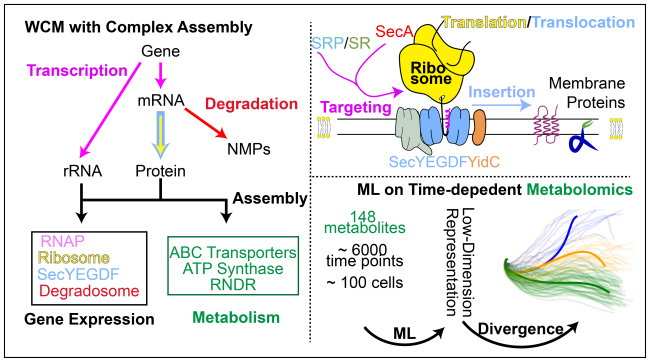
WCM with Complex Assembly
Gene
Transcription
mRNA
Degradation
NMPs
rRNA
Protein
Assembly
RNAP
Ribosome
SecYEGDF
Degradosome
Gene Expression
ABC Transporters
ATP Synthase
RNDR
Metabolism
SRP/SR
SecA
Translation/Translocation
Ribo
some
Targeting
Insertion
Membrane
Proteins
SecYEGDFYidC
ML on Time-depedent Metabolomics
148
metabolites
~ 6000
time points
~ 100 cells
Low-Dimension
Representation
ML
Divergence